Geometry optimisation of vertical axis wind turbine with Gurney flap for performance enhancement at low, medium and high ranges of tip speed ratios

Taurista P. Syawitri[a,b], Yufeng Yao[a*], Jun Yao[a] and Budi Chandra[a]

[a]*Department of Engineering Design and Mathematics, University of The West of England, Bristol BS16 1QY, United Kingdom*

[b]*Department of Mechanical Engineering, Universitas Muhammadiyah Surakarta, Surakarta 57162, Central Java, Indonesia*

*Corresponding author: yufeng.yao@uwe.ac.uk

Highlights

- Geometry of Gurney flap mounted on VAWT is optimised using Taguchi method
- Optimisation considers the effect of rotating blades at different tip speed ratios
- Optimum Gurney flap geometry varies depending on the tip speed ratio
- Maximum performance improvement by Gurney flap is achieved at a lower tip speed ratio
- Performance of VAWT with Gurney flap decreases with the increase of tip speed ratio

Abstract

Optimisation of Gurney flap (GF) geometries mounted on a three-straight-bladed vertical axis wind turbine (VAWT) is evaluated with computational fluid dynamics (CFD) solution and Taguchi method, considering the blade rotating effect at three tip speed ratios (*TSRs*) of low, medium and high ranges. A hybrid RANS-LES model applying stress-blended eddy simulation with transition shear-stress transport turbulence model is adopted. Results analysis confirms that GF geometry optimisation needs to consider multiple rotational blades rather than a single stationary one, owing to different optimum GF geometries and their performances at a different range of *TSR*s. It is found that VAWT with GF can significantly improve the power coefficient at low range *TSR*s (up to 233.19%), but it decreases with the increase of *TSR*s ranges (up to 69.94% and 41.36% at medium and high ranges of *TSR*s, respectively).

Keywords: Vertical Axis Wind Turbine; Gurney Flap; Stress-blended Eddy Simulation; Geometry Optimisation; Taguchi Method.

1. Introduction

Vertical Axis Wind Turbine (VAWT) has received increasing interest in recent years due to its lower cut-in speed, small size in dimensions, and relatively less noise pollution, compared to large-scale Horizontal Axis Wind Turbine (HAWT). Thus, it is more suitable for urban environment applications. In practice, VAWT is easier to install and maintain because its generator and gearbox are located near the ground. In addition, the absence of the yaw mechanism in VAWT can further reduce the complexity of the system and increase turbine reliability, leading to the reduction of total capital cost [1]. In terms of flow physics, VAWT is less sensitive to adjacent turbines' wake flow than HAWT. This characteristic helps VAWT to have better performance than HAWT in urban environments, where both unsteady flows and largely skewed wind conditions are often prevalent and persistent.

Despite of those aforementioned benefits, VAWTs still need further performance improvement to compete with commercial HAWTs, mainly due to their relatively lower efficiency and poorer self-starting capability. In general, there are two methods implemented in the past to improve the VAWT performance. The first method is to use active or passive flow control device to control the dynamic stall of turbine blades and the second method is to use flow augmentation device to increase local wind speed and/or re-direct incoming wind towards the turbine. These two methods have been proven successful, as they can improve the efficiency and self-starting ability of VAWT. The study presented in this paper is purely devoted to the use of dynamic stall control to improve the performance of a three-straight-bladed VAWT model.

Compared to active flow control, passive flow control is a relatively simple and practical solution for VAWT performance enhancement. This is primarily due to the general requirement of an external power source for active flow control, which can add further complexities in product design and manufacturing process, along with additional maintenance costs and operational difficulties. As VAWTs are usually deployed in low wind speed areas such as urban environments, this additional external power requirement can significantly reduce the economic feasibility of VAWTs. Therefore, passive flow control is widely used, as it does not need an external power source.

Among available passive flow control devices, Gurney flap (GF) has been given much attention by many researchers. It is due to its simple geometry modification, low cost in production and better performance improvement, especially at low range of Tip Speed Ratios (*TSR*s) (i.e. the ratio between the wind speed and the speed of the tips of the wind turbine blades, as defined by Equation (1) later). Recent studies [2, 3, 4, 5, 6] have found that GF can significantly improve the lift coefficient whilst having small drag coefficient increase, resulting in considerable power coefficient (C_p) improvement of VAWT. GF can also improve the self-starting ability of VAWT, which will reduce the external power source needed to rotate the turbine initially at a very low incoming wind speed or a low range of *TSR* [4]. Furthermore, GF could improve the VAWT performance at all ranges of *TSR*s operation [4], compared to other passive flow controls such as dimple/cavity [7], vortex generator [8, 9], leading edge serrations [10], winglet [11], or leading edge micro-cylinders [8], as these alternative solutions can merely increase the VAWT performance over a narrow range of *TSR*s. According to a previous study [6], it was evident that the ability of GF to improve the VAWT performance can be varied, depending on GF geometry details. Therefore, geometry optimisation can be very crucial in the design of GF to be implemented in VAWT. It is known that both the blade rotating effect and blade-to-blade interaction have significant impacts on the performance of VAWT. Moreover, VAWT can be operated at typically three different ranges of *TSR*s, namely, low range of *TSR*s, medium range of *TSR*s and high range of *TSR*s. Within each range of *TSR*s, flow behaviour around VAWT will be quite differently. Based on the evaluation of NACA 0021 aerofoil VAWT at low range of *TSR*s by Castelli et al. [12], it was found that during the operation, VAWT blades can experience higher angle of attack (*AoA*) up to 27.7°, which is beyond the stall angle of a static aerofoil (normally +15°/-15°). This causes very small positive and sometimes even negative torque productions, leading to the poor self-starting ability of VAWT at low wind speed or low *TSR*s operation condition [13]. At medium range of *TSR*s, VAWT blades will have a small increment of *AoA* beyond static stall angle compared to low range of *TSR*s (up to 10.3° higher than stall angle of a stationary aerofoil). As a result, the flow can be considered mostly attached to blade surfaces and the level of flow unsteadiness of VAWT is decreased accordingly. At this medium range of *TSR*s, optimum *TSR* operation can be obtained due to strong shed wake of the turbine and significant induction velocities [14]. Lastly, VAWT will have less *AoA* increment beyond the static stall angle at high range of *TSR*s (up to 5° higher than stall angle of a stationary aerofoil), compared to low and medium ranges of *TSR*s. Even though the turbine can still operate at the ranges of no static stall condition, the power production may decrease, due to the fact that the rotor can act as a solid wall obstruction at a high rotational speed [15]. The higher rotational speeds will also induce high vibrations, drag increases and tip losses in VAWT, resulting in lower power generation of VAWT at high range of *TSR*s [16].

Consequently, it is crucial to conduct the optimisation of a full VAWT configuration (i.e. considering blade rotating effect and blade-to-blade interaction) at these three ranges of *TSR*s (i.e. low, medium and high ranges of *TSR*s) so that the GF geometry can be modified accordingly to generate the optimum solution for VAWT performance improvement at all ranges of *TSR*s. Nonetheless, previous studies on the use of GF in VAWT have primarily focused on performing geometry optimisation of a single stationary aerofoil and at a narrow range of *TSR*s [4, 6]. Although there is a study that has performed geometry optimisation of a full VAWT configuration at all ranges of *TSR*s [5], it only focused on how geometry parameters (e.g. the height (*H*) and mounting angle (θ_{GF})) behave at different *TSRs* without evaluating the optimum value at each range of *TSR*s and discussing possible reasons behind. Therefore, it is necessary to perform geometry optimisation of GF for a full VAWT configuration at all ranges of *TSR*s.

Furthermore, due to the constraint of key parameters in GF geometry evaluation, previous studies were often limited, e.g. merely focussing on the height and mounting angle optimisations [4, 5, 6]. On the other hand, the evaluation of other GF geometry parameters in a stationary aerofoil modification has been widely performed within the aerodynamic community, including GF position from the trailing edge (*s*) [17]. It was found that this parameter also has significant effect on aerofoil performance. However, it is still unclear on its effectiveness for multiple rotating blades such as VAWT.

Additionally, some previous studies [4, 5, 6] performed GF geometry optimisation merely for one parameter variation at a time. Hence, there is no information about which parameter of GF gives the highest or the lowest impact on the performance improvement of VAWT. In the meantime, a multiple-parameter optimisation method based on a fractional design called Taguchi method [18] has been utilised to optimise straight upstream deflector geometry, leading edge serration and helical blade for performance enhancement of VAWT previously [19, 20]. This method can largely reduce the computational cost as it allows the optimisation design to be performed with a fractional design rather than a complete factorial design [19]. Thus, it is more suitable for investigating the sensitivity of each parameter to the goal of the design [21], while considering two robust characteristics as "uniformity and decentralisation, orderliness and comparable". "Orderliness and comparable" can ensure that the experimental results comparison is convenient, whilst "uniformity and decentralisation" can establish uniformly scattered sample points over the domain [21]. This is one of advantages of the Taguchi method compared to other fractional design methods such as Latin Hypercube Sample (LHS), as the sample points in LHS are often random [21]. Hence, even if the number of computations and the interval of parameters are all pre-fixed, the LHS results will still be different at a different time instance [21]. Therefore, it is not suitable to use this method for studying the sensitivity of each parameter to the design goal.

To overcome all of the shortcomings described above, this study attempts to perform the optimisation of GF geometry for a full VAWT configuration, by considering the blade rotating effect and blade-to-blade interaction at all ranges of *TSR*s over a wider range of GF parameters. In addition to GF height and mounting angle as previously studied [4, 5, 6], the GF position from the trailing edge is also evaluated. Note that only one *TSR* is chosen as a representative value for each range of *TSR*s, i.e. *TSR* = 1.44 for low range of *TSR*s, *TSR* = 2.64 for medium range of *TSR*s and *TSR* = 3.3 for high range of *TSR*s. This is because VAWT behaves quite similarly at the same range of *TSR*s operation [22].

Taguchi method [18] is adopted to perform simultaneous optimisation of three different GF geometry parameters (i.e. height, mounting angle and position from the trailing edge). To the authors' knowledge, this is the first kind of work to be attempted for multiple-parameter GF optimisation applied to a VAWT configuration, as previous optimisations [4, 5, 6] were merely for one parameter variation at a time. Furthermore, this study only considers the maximum power coefficient of VAWT as the goal of the optimum design. Therefore, other design factors, such as structure vibration and noise, are not considered in this study.

A three-straight-bladed VAWT model is adopted and the investigation will focus on a 2D mid-plane cutting through the 3D configuration, applying computational fluid dynamics (CFD) simulation. Hence, the results of this present study are only appropriate for VAWT with a high aspect ratio where the blade tip effect is relatively insignificant. Reynolds averaged Navier-Stokes equations (RANS) are solved together with a stress-blended eddy simulation (SBES) turbulence model along with transition shear-stress transport (TSST), so-called a hybrid RANS-LES approach. All CFD simulations are carried out using ANSYS Fluent v19 [23].

2. Description of Bare VAWT and Gurney Flap Geometry

2.1. Bare VAWT

A three-straight-bladed Darrieus VAWT equipped with NACA 0021 aerofoil, previously examined by Castelli et al. [12] experimentally and numerically, is adopted as a baseline bare VAWT configuration in this study with parameter details given in Table 1. It can be seen from the study of Castelli et al. [12] that the position of the spoke-blade connection between their simulations and experiments is somehow different, and there is no clear explanation for this difference. It is very likely that Castelli et al. [12] have altered the spoke-blade connection position in their experiments from 0.25 *c* to 0.5 *c* to ease the experimental procedure and perform some post-test corrections to take into account the spoke drag due to this change. Furthermore, Castelli et al. [12] have evaluated this VAWT at U_∞ = 9 *m/s* with *TSR*s ranging between 1.44 and 3.3. The turbine rotational speed is calculated based on Equation (1) as,

$$TSR = \frac{\omega_r R}{U_\infty}, \tag{1}$$

Table 1. Main geometrical parameters of Castelli et al. [12] model.

Parameters	**Simulation**	**Experiment**
Turbine diameter (D_{rotor} (*mm*))	1030	1030
Turbine height (H_{rotor} (*mm*))	1000 (for 2D simulation)	1456.4
Turbine swept area (A_s (m^2))	1.03	1.236
Number of blades (*N* (-))	3	3
Blade profile	NACA 0021	NACA 0021
Chord length (*c* (*mm*))	85.8	85.8
Trailing edge thickness (*mm*)	0.3792	0.3792
Spoke-blade connection	0.25 of chord length	0.5 of chord length
Solidity (σ (-))	0.5	0.5
Aspect ratio	1.4	1.4

2.2. Gurney Flap

In this study, a bare VAWT model is modified by mounting a GF at the trailing edge of NACA 0021 aerofoil. The GF has a rectangular shape with a fixed thickness (*l*) (0.33% of aerofoil chord) and other parameters such as height (*H*), mounting angle (θ_{GF}) and distance from the trailing edge (*s*) are varied for geometry optimisation studies (see Figure 1). The chosen GF thickness is based on the finding of a previous study by Mohammadi et al. [24].

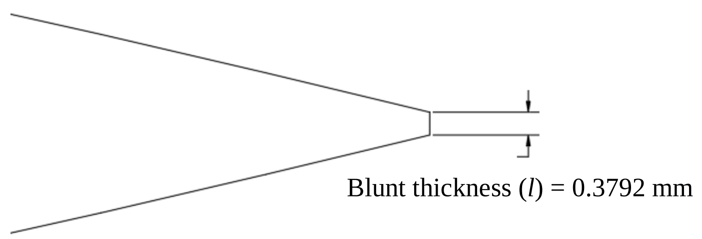

(a)

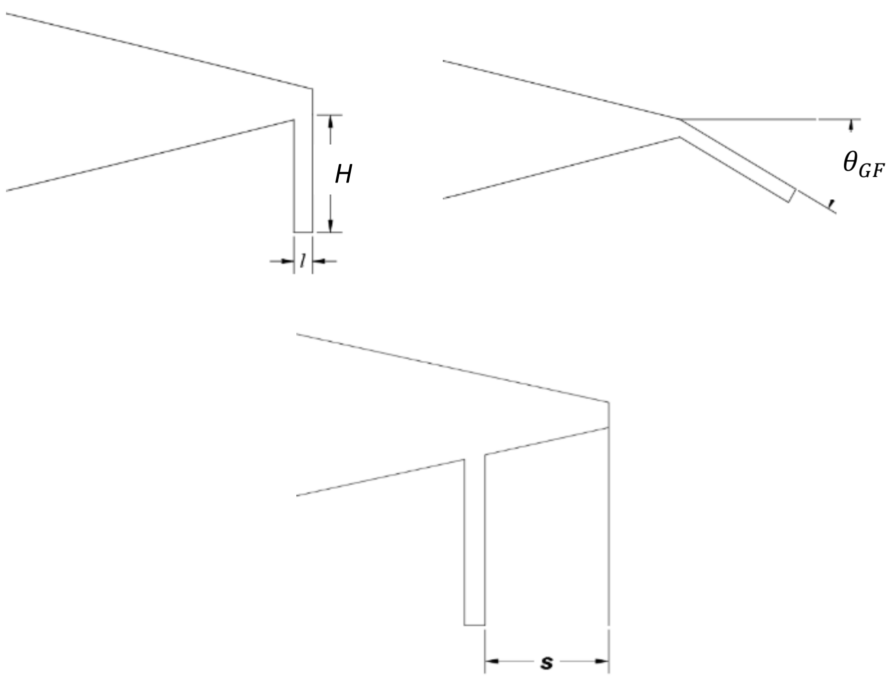

(b)

Figure 1. Visualisation of (a) clean NACA 0021 aerofoil, (b) NACA 0021 with GF geometry variations (note sketches are not in scale).

3. CFD Simulation Process

3.1. Domain Decomposition and Grid Generation

A C-grid type of mesh generation is adopted, as it can produce quality structure grids for blades quipped with GF geometry. The computational domain is at first decomposed into three sub-domains, called the far-field, rotating core and control sub-domains (see Figure 2). A C-grid with a rectangular enclosure is applied for the far-field sub-domain, a non-rotating sub-domain surrounding the interior rotating core sub-domain. Zhu et al. [25] suggested that this C-grid has 25*R* in radius and the rectangular enclosure has 30*R* in the stream-wise direction from the centre of the blade rotating axis to the exit plane. This sub-domain is further divided into six regions (for details, see [26]) to facilitate smoother mesh generation. A structured grid with 18240 quadrilateral cells is finally generated within this sub-domain [26].

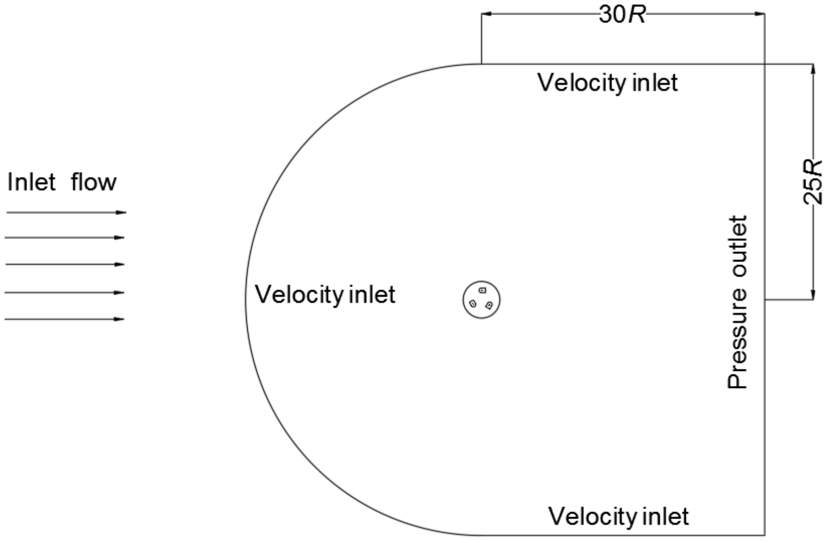

(a)

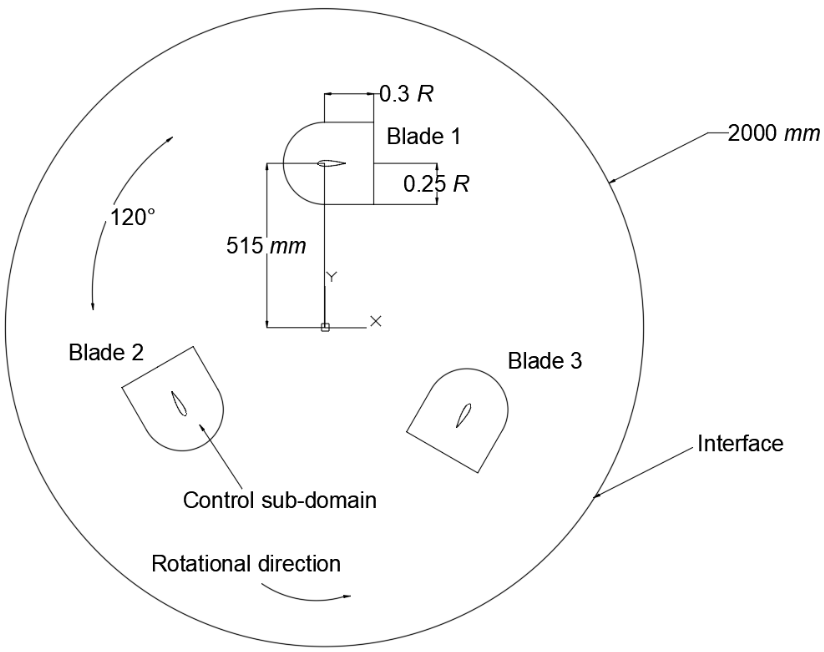

(b)

Figure 2. 2D computational domain (all dimensions are measured in *mm*) of the present study, (a) overview of the whole computational domain and (b) details of the rotating core and control sub-domains (note sketches are not in scale).

To implement the revolution of turbines, a circular domain with 2000 *mm* in diameter called the rotating core sub-domain is adopted within the computational domain. This sub-domain rotates in an anti-clockwise direction around the rotating turbine axis at a pre-defined rotational speed. A total of 22527 quad-dominant cells is generated in this sub-domain [26]. A "fluid-fluid" interface is set up at the boundary intersection between the far-field and rotating core sub-domains to ensure the continuity of fluid flow crossing these two sub-domains. This is accomplished by creating interface boundary conditions at the boundary intersection between the far-field and rotating core sub-domains for each sub-domain. Then, a mesh interface is created to connect these interface boundary conditions.

The remaining sub-domains are called control sub-domains (see Figure 2 (b)) and they are used to generate grids around three blades. Three control sub-domains with inserted blades are located inside the rotating core sub-domain and separated by 120° angular distance between two adjacent blades. The C-shape with 0.25R in radius and 0.3R in length from the centre of the blade is applied in each control sub-domain. Noting that, the boundaries between control sub-domains and rotating core sub-domain are frozen and treated as "interior" to ensure the continuity of the fluid flow. A total of 49680 structured quadrilateral cells are generated in each control sub-domain, with fine grids in the near-wall region of the trailing edge of blade (see Figure 3 in details) and coarse grids away from the wall. To satisfy the criteria of the TSST turbulence model, a non-dimensional wall distance $y^+ < 1$ is adopted whilst generating the first layer grid height near the wall of the blades.

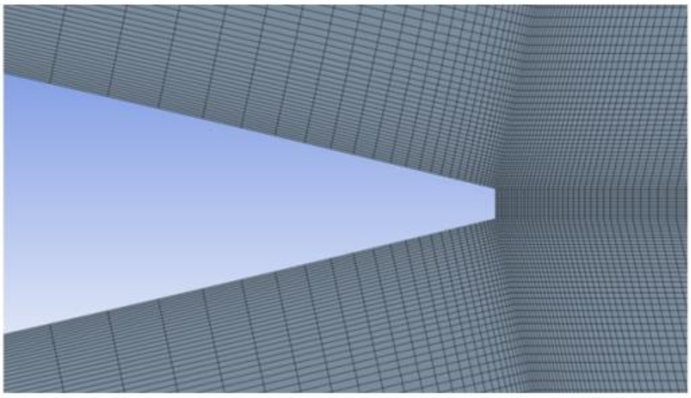

(a) Clean aerofoil

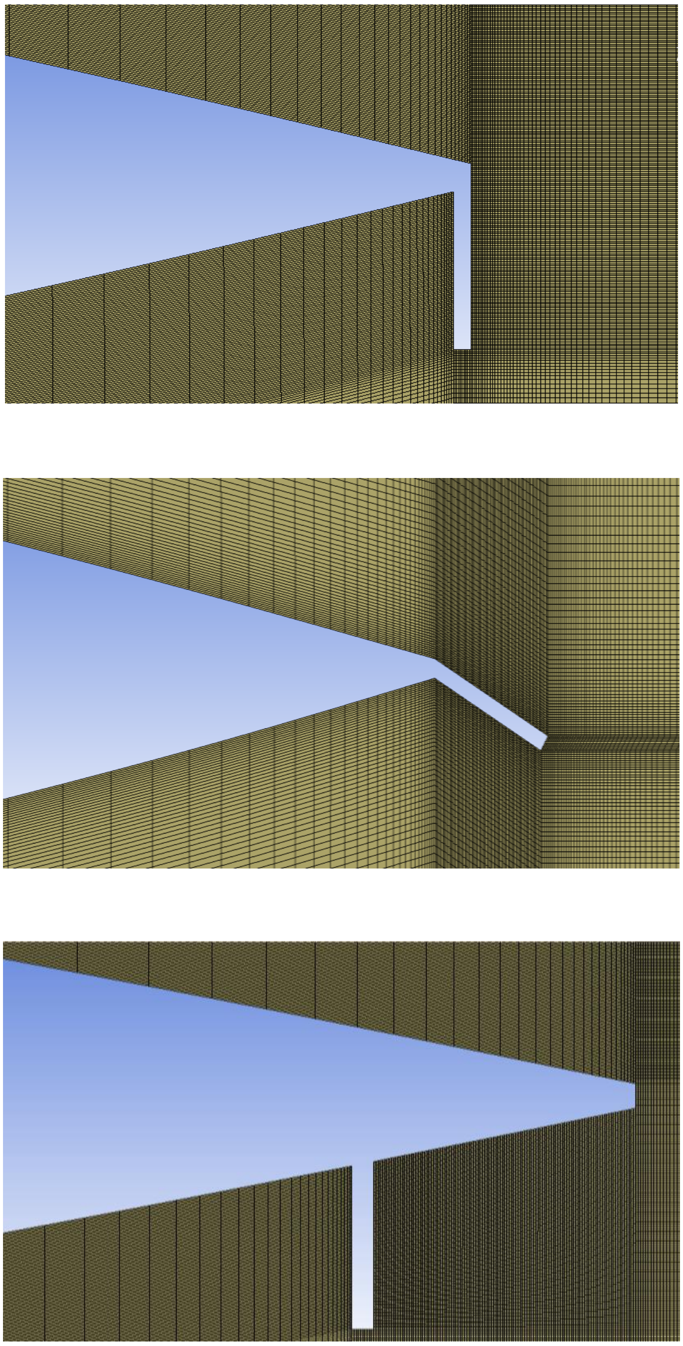

(b) GF aerofoil

Figure 3. Grid details around the trailing edge of the blade (not in scale).

3.2. Turbulence Model

This study applies a relatively new hybrid RANS-LES turbulence model called stress-blended eddy simulation (SBES). This model was initially proposed by Menter [27] mainly to resolve the issue of Grid Induced Separation (GIS) that usually appears in previous hybrid RANS-LES approaches such as Delayed-Detached Eddy Simulation (DDES) and Improved-Detached-Delayed Eddy Simulations (IDDES) when the mesh is refined in the boundary layer region. Such a GIS is mainly due to the fact that there is improper balancing between RANS and LES turbulence contents caused by the influence of the LES grid limiter on the RANS model. It is also caused by the tendency of "slow" transition from the RANS to the LES zones in separating shear layer (SSL) region [28] with no clear differentiator between the RANS and LES regions.

The SBES model improves the "clearness" between the RANS and the LES zones by visualising the shielding function, and thus revises it in the shielded DES (SDES) SST model to protect the RANS boundary layers whilst automatically switches to an existing algebraic LES model in the LES zone [27]. SBES introduces an explicit function to switch to an algebraic LES whilst maintaining the blending function the same as that of the shielding function in SDES (f_{SDES}), whilst disables it in the LES zone where $f_{SDES} = 0$. As a result, the Reynolds stress tensor and eddy viscosity equations are changed to

$$\tau_{i,j}^{SBES} = f_{SDES}\tau_{i,j}^{RANS} + (1 - f_{SDES})\tau_{i,j}^{LES}, \tag{2}$$

$$\upsilon_t^{SBES} = f_{SDES}\upsilon_t^{RANS} + (1 - f_{SDES})\upsilon_t^{LES}, \tag{3}$$

where $\tau_{i,j}^{SBES}$, $\tau_{i,j}^{RANS}$ and $\tau_{i,j}^{LES}$ are turbulence Reynolds stress tensors and υ_t^{SBES}, υ_t^{RANS} and υ_t^{LES} are turbulence kinematic viscosities. SBES model also reduces the enforced turbulence stress level of the LES model. Hence, this model can change rapidly from the RANS to the LES function in SSL region, producing better, realistic, and consistent solutions. Furthermore, this turbulence model allows a "switch" between RANS zone and LES zone to be predictable even on a coarser grid, but other Detached Eddy Simulation (DES) models such as DDES or IDDES cannot do so.

The implementation of the SBES model with TSST in CFD modelling of VAWT has been evaluated in the previous studies [26, 29]. It was found that this model could largely reduce the power coefficient discrepancies between CFD predictions and experiment measurements at all *TSR*s operations, whilst the unsteady RANS (URANS) model could not achieve. Additionally, the hybrid RANS-LES turbulence models such as SBES could predict dynamic stall behaviour more accurately than URANS turbulence models implicated by further vortex shedding away from blade wall and trailing edge. They can also predict weak trailing edge vortex roll up at high ranges *TSR*s whilst URANS turbulence models only show weak vortex shedding around the trailing edge, but not the roll up behaviour [29].

3.3. Computational Settings

In this study, both pressure-velocity coupling and second-order accuracy numerical scheme for both temporal and spatial discretisation are implemented to solve the Navier-Stokes equations in a hybrid RANS-LES manner. Due to the use of a hybrid RANS-LES turbulence model, bounded central differencing (BCD) is applied for momentum spatial discretisation. The residual convergence criteria for the inner loop is set equal to or less than 10^{-6}. As discussed in the previous study [30], a total of 40 sub-iterations per time step is adopted to reduce turbulence kinetic energy (TKE) residual by order of 10^{-4}. The time step is set to be the lapse time of blades making a 1° rotation, which has been proved sufficient for VAWT simulations [26, 29].

It is known that for VAWT simulation, it is necessary to achieve a statistically converged flow field before collecting data samples. Several studies have suggested that the simulation must achieve the 'converged' performance until the variation of power coefficient (C_p) or moment coefficient (C_m) between two neighbouring revolutions is at least less than 1% [12] or even more stringent criteria of 0.1% [31] before collecting data samples. The evaluation of blade revolution convergence by the present authors has found that a total of 34 revolutions is necessary before the differences of C_m between two neighbouring revolutions are less than 0.1% for SBES with TSST turbulence model [29]. Therefore, data samples are collected from a simulation of the 35th revolution in this study.

3.4 Model Validation

The grid independence and model validation studies have already been documented in works of the present authors [26, 29]. As mentioned in the previous study [26], three grid resolutions from coarse, medium, to finer meshes, each having 87, 174 and 348 cells around the blade, were considered for grid independence study. The results illustrated that the instantaneous moment coefficient (C_{mi}) changes along azimuthal positions have shown a small difference between the medium and the fine grids whilst the coarse grid could not produce satisfying instantaneous moment coefficients [26].

The model validation study also showed that CFD simulations adopting SBES with TSST turbulence model can generate better predictions of averaged power coefficient over one blade revolution ($C_{p\text{-}ave}$), compared to URANS realisable k-ε turbulence model with enhanced wall treatment (RKE) that was used in the study of Castelli et al. [12] among all ranges of *TSR*s operation [26, 29]. In particular, SBES with TSST model is found superior compared to RKE model at low range of *TSR*s. Whilst CFD simulation with RKE model generates nearly 441% error of $C_{p\text{-}ave}$ prediction compared to experimental data at low range of *TSR*s, SBES with TSST model can largely reduce this discrepancy to be just less than 52% [26]. At medium and high ranges of *TSR*s, SBES with TSST model also produces small discrepancy to be less than 1%, whilst the RKE model produces about 16% discrepancy on average compared to experimental data [26]. Therefore, SBES with TSST model will be used for further simulations and optimisations presented below.

4. Optimisation Method

To investigate the effect of different GF geometry parameters on the VAWT performance (e.g. the power coefficient), numerical experiments can be adopted to study the effect of multiple parameters simultaneously. However, the study of all possible parameters combined can be quite challenging because it needs a complete factorial design that is not feasible for investigation with a large number of parameters. Moreover, the time and resources can be very demanding. Hence, this study adopts a fractional design investigation based on the Taguchi method and its applications [18, 19, 20].

Taguchi method is an optimisation method that Taguchi developed in order to improve the quality of manufactured goods. The main principle of this method is based on a so-called quality loss function, expressed by the deviation of parameter from its target value [18]. Note that the parameters are divided into control and noise parameters in the Taguchi method. The control parameters are used to determine the optimum condition, whilst noise parameters show the deviation of the system from its target value and are not controlled [19]. The influence of the noise parameters on the system performance is used to determine the optimisation, and it can be calculated using the signal to noise (S/N) ratio. In the Taguchi method, there are three kinds of S/N ratio functions, namely the larger-the-better (LB), the nominal-the-better (NB) and the smaller-the-better (SB), respectively [19, 20]. The choice of the S/N ratio function mainly depends on the target value of the evaluation.

After determining the control and noise parameters, a matrix of numerical experiments can be designed based on orthogonal arrays of the control and noise parameters. This matrix is used to guide numerical experiments until the results are obtained for each test cycle. The optimum value of each control parameter is then determined by using the S/N ratio. As this study aims to generate higher power output, the larger-the-better S/N ratio function to maximise the target value of power output is applied. This LB S/N ratio can be obtained by using the following Equation (4) as [18]:

$$S/N = -10log\left(\frac{1}{nc}\sum_{i}^{nc} 1\frac{1}{I_i^2}\right), \quad (4)$$

where nc is the total number of observed cases, I_i is the value of observed performance indicator of each individual case (in present study, this value is the averaged power coefficient of VAWT obtained from CFD simulation) and i is the index of simulation case.

As mentioned above, this study will evaluate the effect of three GF geometry parameters on the VAWT performance, including GF height, mounting angle and position from the trailing edge. Therefore, before applying the Taguchi method, precursor studies are carried out to evaluate the effects of GF height, mounting angle, and distance to trailing edge variations to identify appropriate ranges, thus avoiding an unnecessarily large number of test cases during the optimisation stage. This is necessary to avoid the enormous computational cost of CFD simulation. In this study, it takes about 48 hours on average to simulate one case using a high-spec workstation with 2 CPUs @ 2.2 GHz, 128 GB RAM. During these precursor studies, only one parameter is varied at a time, while the other two parameters are fixed based on the optimum values of previous studies [6, 17, 32].

4.1. Range values of the height of GF

To determine the range of GF height for optimisation, pre-evaluation is conducted by varying the GF height from 1% to 4% c with a fixed mounting angle of 90° and a fixed position at 0% c from the trailing edge. Figure 4 (a) shows the effect of GF height with regard to the averaged power coefficient over one blade revolution at all three ranges of *TSR*s. It can be seen that the $C_{p\text{-}ave}$ increases with the increase of GF height until reaching an optimum value at H = 3% c at all three ranges of *TSR*s. After that, the $C_{p\text{-}ave}$ decreases, indicating GF height larger than 3% c will not further improve the VAWT performance. Hence, further study only evaluates three GF heights for optimisation, i.e. H = 2%, 3% and 4% c.

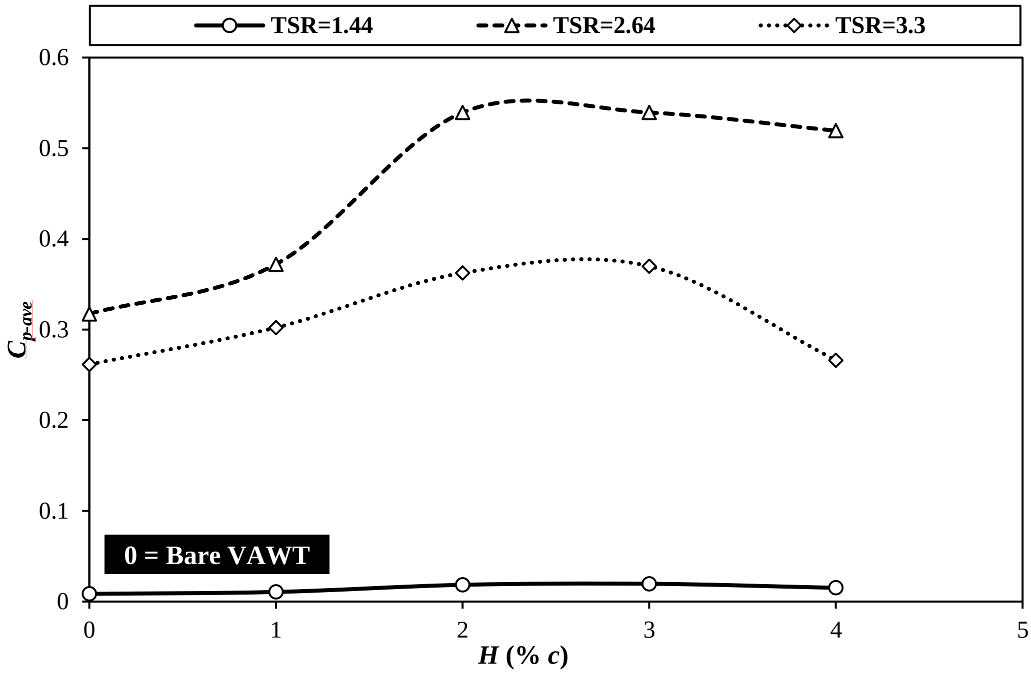
TSR=1.44
TSR=2.64
TSR=3.3
C_{p-ave}
0 = Bare VAWT
0
0.1
0.2
0.3
0.4
0.5
0.6
0
1
2
3
4
5
H (% *c*)

(a)

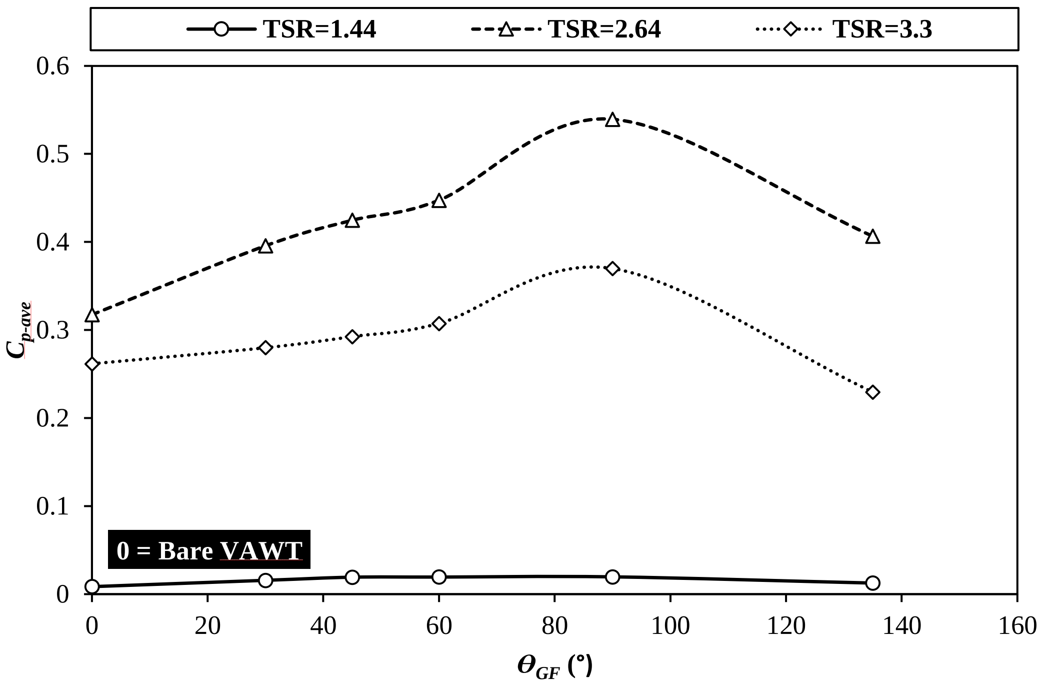
TSR=1.44
TSR=2.64
TSR=3.3
C_{p-ave}
0 = Bare VAWT
0
0.1
0.2
0.3
0.4
0.5
0.6
0
20
40
60
80
100
120
140
160
θ_{GF} (°)

(b)

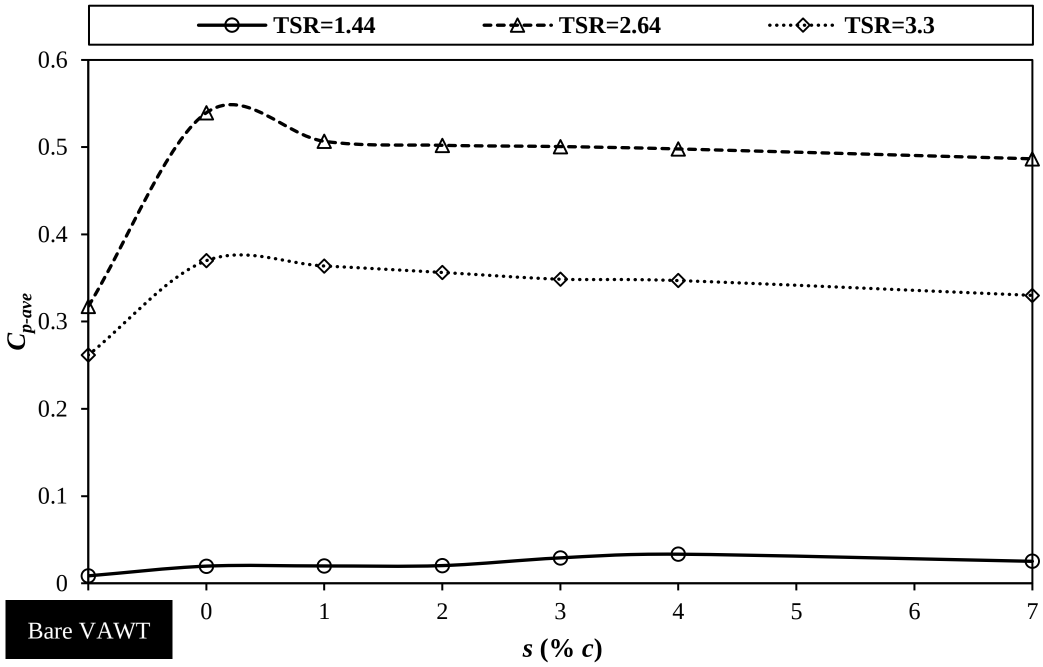

(c)

Figure 4. Comparison of $C_{p\text{-}ave}$ for a VAWT with and without GF at all three ranges of *TSR*s against (a) GF heights, (b) GF mounting angles and (c) GF positions from the trailing edge.

4.2. Range values of the mounting angle of GF

In order to determine the range of GF mounting angle, the mounting angle is varied from 30° to 135°. The GF height and position from the trailing edge are fixed at 3% *c* and 0% *c*, respectively. As illustrated in Figure 4 (b), the $C_{p\text{-}ave}$ has been enhanced at all three ranges of *TSR*s as the mounting angle increases. The maximum improvement is achieved for a mounting angle of 90°. Further increase of mounting angle does not enhance the $C_{p\text{-}ave}$. Therefore, three mounting angles of θ_{GF} = 60°, 90° and 135° are chosen for GF geometry optimisation.

4.3. Range values of the position from the trailing edge of GF

In this pre-evaluation, the position from the trailing edge of GF is varied from 0% to 7% *c* with a fixed GF height and mounting angle of 3% *c* and 90°, respectively. Figure 4 (c) shows that at medium and high ranges of *TSR*s the maximum performance comes from a GF position at the trailing edge, i.e. s = 0% *c*. Whilst all GF positions tested can enhance the $C_{p\text{-}ave}$ compared to a bare VAWT, the increase of the GF distance to the trailing edge will produce slightly decreased $C_{p\text{-}ave}$ at both medium and high ranges of *TSR*s (see Figure 4 (c)). However, different behaviours happened at low range of *TSR*s. As the GF position moves away from the trailing edge, the $C_{p\text{-}ave}$ increases compared to GF at the trailing edge until reaching its optimum value at 4% *c* from the trailing edge. After this position, the $C_{p\text{-}ave}$ decreases. Further explanation about this behaviour will be discussed later in Section 5.5. Based on these pre-evaluations, three distances to the trailing edge are chosen as 0%, 4% and 7% *c* to include those influential positions at all ranges of *TSR*s.

5. Results and Discussion

5.1. Geometry Optimisation

Following the GF geometry variants described above, a case study matrix is proposed based on the Taguchi method. As this study aims to optimise three different geometrical parameters of GF (i.e. height, mounting angle and position from the trailing edge) with each parameter having three different values (see Table 2), the study will form a 3 × 3 × 3 matrix with a total of 27 cases (see Table 3). Noting that VAWT performance has different behaviours at different ranges of *TSR*s, so that this investigation is performed at all three different ranges of *TSR*s with *TSR* = 1.44 representing low range of *TSR*s, and *TSRs* = 2.64 and 3.3 for medium and high ranges of *TSR*s, respectively. Therefore, there will be a total of 81 cases to be investigated (i.e. each *TSR* has 27 cases).

Table 2. Details of GF geometry parameters and levels of studies.

Parameter	**Level**		
	1	2	3
H	2% *c*	3% *c*	4% *c*
θ_{GF}	60°	90°	135°
s	0% *c*	4% *c*	7% *c*

Table 3. Matrix of case studies for each *TSR*.

Run	**H (% c)**	**θ_{GF} (°)**	**s (% c from the trailing edge)**
1	2	60	0
2	2	60	4
3	2	60	7
4	2	90	0
5	2	90	4
6	2	90	7
7	2	135	0
8	2	135	4
9	2	135	7
10	3	60	0

11	3	60	4
12	3	60	7
13	3	90	0
14	3	90	4
15	3	90	7
16	3	135	0
17	3	135	4
18	3	135	7
19	4	60	0
20	4	60	4
21	4	60	7
22	4	90	0
23	4	90	4
24	4	90	7
25	4	135	0
26	4	135	4
27	4	135	7

Table 4 shows the predicted $C_{p\text{-}ave}$ of 27 cases for each pre-defined *TSR*. The results indicate that optimum $C_{p\text{-}ave}$ has shown different increments for each range of *TSR*s compared to bare VAWT. By choosing certain geometry parameters, the $C_{p\text{-}ave}$ increment can be around 233.19% higher than a bare VAWT at low range of *TSR*s. Meanwhile, this increment is reduced to 69.94% and 41.36%, respectively, at medium and high ranges of *TSR*s. Moreover, the optimum geometry will differ between the low range of *TSR*s and the medium and high ranges of *TSR*s.

Based on the mean *S/N* ratio tabulated in Table 5, at medium and high ranges of *TSR*s, the largest mean *S/N* ratio for the GF height and mounting angle is obtained at level 2, whilst for GF position from the trailing edge, it is obtained at level 1. This means that the optimum GF geometry at these ranges of *TSR*s is a GF configuration with H = 3% c, θ_{GF} = 90° and s = 0% c. However, there is a change in optimum geometry parameter for GF position from the trailing edge at low range of *TSR*s. The mean *S/N* ratio for the parameter s reaches its maximum value at level 2 at the low range of *TSR*s with the same optimum level for the other two parameters. Hence, the optimum GF geometry is a GF configuration with H = 3% c, θ_{GF} = 90° and s = 4% c at low range of *TSR*s. The possible reason behind of this behaviour will be explained later in Section 5.5.

Table 4. C_{p-ave} values of all 81 cases at all ranges of *TSR*s (***bold and italic fonts*** are used for the optimum cases).

Run	*TSR* =1.44		*TSR* = 2.64		*TSR* = 3.3	
	C_{p-ave}	C_{p-ave} increment (%)	C_{p-ave}	C_{p-ave} increment (%)	C_{p-ave}	C_{p-ave} increment (%)
1	0.0179	110.38	0.3693	16.33	0.2940	12.37
2	0.0189	122.09	0.3198	0.75	0.2327	-11.06
3	0.0108	27.54	0.3124	-1.59	0.2265	-13.43
4	0.0185	117.25	0.5394	69.93	0.3624	38.51
5	0.0267	213.58	0.4873	53.51	0.3020	15.40
6	0.0133	56.20	0.4756	49.84	0.2937	12.23
7	0.0112	31.48	0.4019	26.62	0.2176	-16.84
8	0.0189	122.53	0.3587	13.00	0.1692	-35.33
9	0.0096	13.00	0.3493	10.03	0.1641	-37.28
10	0.0194	128.36	0.4474	40.95	0.3075	17.51
11	0.0205	141.49	0.3904	22.97	0.2449	-6.40
12	0.0110	29.20	0.3810	20.03	0.2389	-8.68
13	0.0196	130.94	***0.5394***	***69.94***	***0.3699***	***41.36***
14	***0.0283***	***233.19***	0.4980	56.88	0.3470	32.63
15	0.0163	91.24	0.4866	53.31	0.3301	26.14
16	0.0126	47.85	0.4065	28.07	0.2295	-12.30
17	0.0232	172.49	0.3584	12.92	0.1806	-30.97
18	0.0115	35.14	0.3490	9.96	0.1749	-33.15
19	0.0135	58.27	0.3286	3.51	0.1835	-29.88
20	0.0147	73.28	0.2878	-9.34	0.1241	-52.59
21	0.0089	4.54	0.2809	-11.50	0.1205	-53.95
22	0.0152	78.43	0.5193	63.61	0.2663	1.76
23	0.0214	151.74	0.4766	50.16	0.1943	-25.72
24	0.0124	46.22	0.4653	46.57	0.1888	-27.85
25	0.0093	9.33	0.3319	4.56	0.1133	-56.70
26	0.0151	77.18	0.2855	-10.05	0.0879	-66.39
27	0.0078	-8.68	0.2776	-12.53	0.0850	-67.50

It is also noticed that the significance of each parameter on the predicted C_{p-ave} of VAWT behaves differently at a different range of *TSR*s. According to the deviation of *S/N* ratio (denoted by Δ thereafter, i.e. Δ = the highest average response characteristic value – the lowest average response characteristic value) for levels of specific parameter and the parameter rank by Taguchi analysis (see Table 5), the GF position from the trailing edge at low range of *TSR*s has the most significant effect on the C_{p-ave} of VAWT, followed by the mounting angle and the height of GF, respectively. This seems reasonable as the change of GF position at low range of

TSRs has a considerable effect on $C_{p\text{-}ave}$ improvement (see, e.g. Figure 4 (c)). The averaged moment coefficient ($C_{m\text{-}ave}$) at low range of TSRs indicates that changing the position of GF can increase this value around 32.22%. Meanwhile, changing the height and mounting angle of GF can only increase the $C_{m\text{-}ave}$ values by 14.03% and 18.37%, respectively.

However, the most significant parameter at the medium and high ranges of TSRs is the mounting angle, followed by the height and position of GF. The reason that the mounting angle of GF has more effects on the change of $C_{p\text{-}ave}$ value compared to the height of GF at all ranges of TSRs is likely due to the fact that in this study, the chosen variation of the height of GF does not generate significant change in $C_{p\text{-}ave}$ value, as the performance of VAWT with GF is already very close to its optimum value.

Table 5. Response of Signal to Noise Ratios (i.e. the large-is-better) after applying Taguchi analysis.

Level	*TSR* = 1.44			*TSR* = 2.64			*TSR* = 3.3		
	Parameter			Parameter			Parameter		
	H	θ_{GF}	s	H	θ_{GF}	s	H	θ_{GF}	s
1	-36.25	-36.78	-36.66	-8.076	-9.301	-7.448	-12.27	-13.59	-12.17
2	-35.33	-34.77	-33.81	-7.454	-6.056	-8.481	-11.68	-10.84	-14.25
3	-38.03	-38.07	-39.14	-9.098	-9.270	-8.698	-16.99	-16.51	-14.52
Δ	2.69	3.30	5.33	1.645	3.245	1.250	5.30	5.68	2.36
Rank	3	2	1	2	1	3	2	1	3

5.2. *General Effect of GF*

As shown in Figure 4 (a) to (c) previously, the introduction of GF can generally increase the power coefficient of VAWT at all ranges of TSRs. This confirms that GF can be applied as a device to improve the VAWT performance at all ranges of TSRs. It is mainly due to the ability of GF to mitigate the negative moment coefficient production, as illustrated in Figure 5 (a). Moreover, the presence of GF can ease the deep stall of turbine blades, which is evident by a slower declining rate in the C_{mi} curve after reaching its maximum peak, as seen in Figure 5 (a).

In order to further understand the effect of VAWT blades mounted with GF on turbine performance, instantaneous lift coefficient (C_{li}) and drag coefficient (C_{di}) of one selected blade (blade 1 is used here) over one rotation cycle are depicted in Figure 5 (b) and Figure 5 (c), respectively. It shows that the introduction of GF can reduce the fluctuation amplitude of C_{li} and delay the sudden increase of C_{di} at an azimuthal position of about 90°. This confirms that the GF can ease the deep stall of turbine blades. The unsteady behaviour of C_{li} and the rapid increment of C_{di} also suggest that the VAWT will start to experience the stall between azimuthal positions of 60°-100°, approximately.

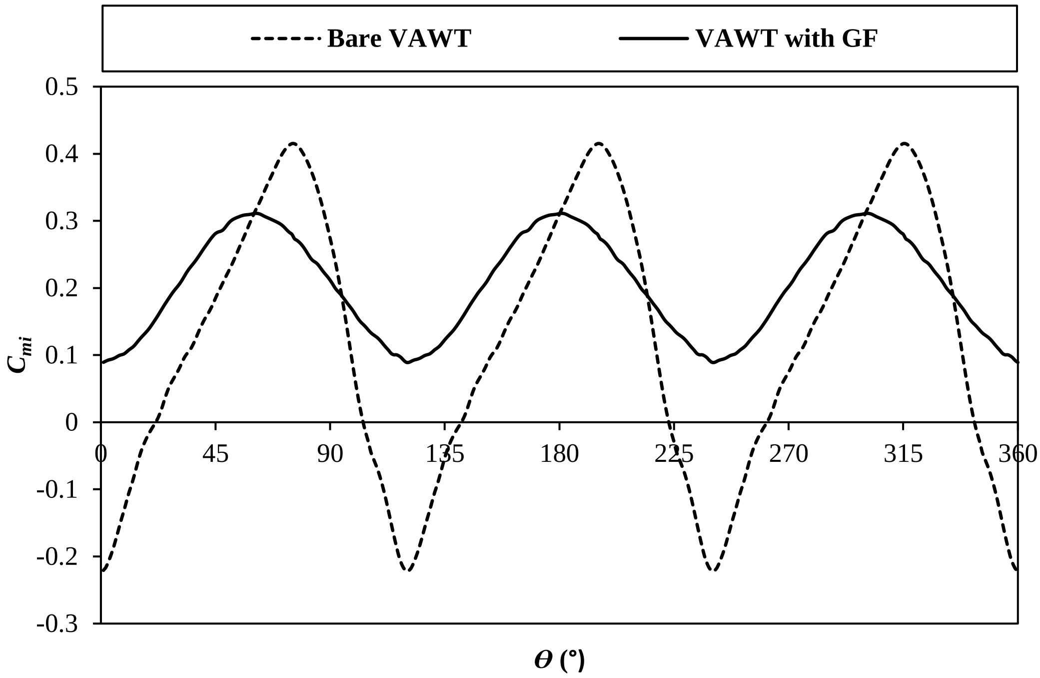

(a)

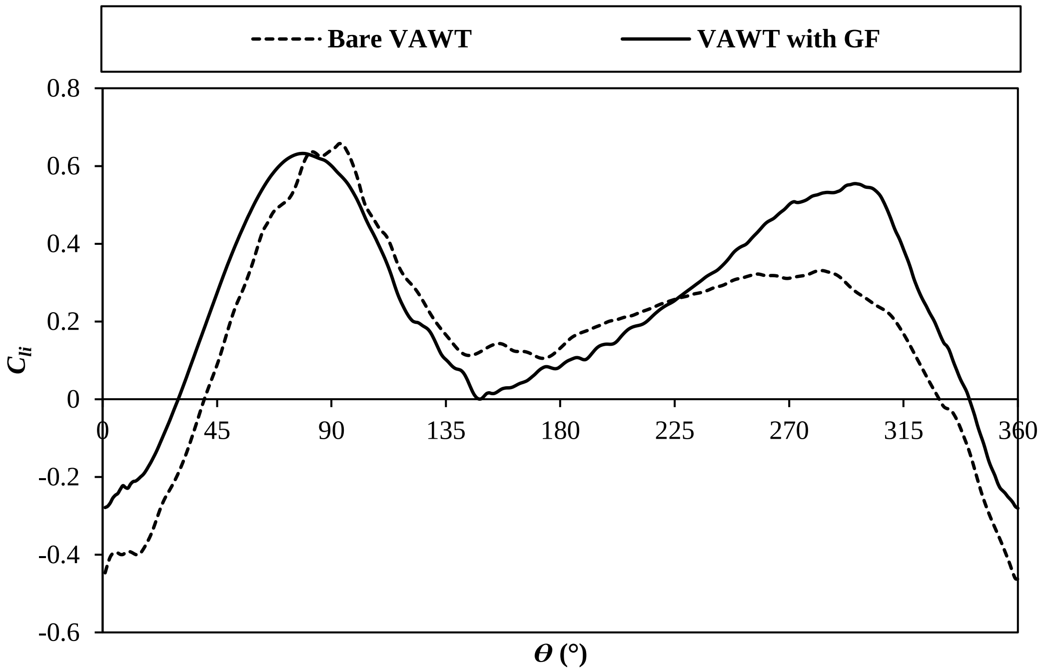

(b)

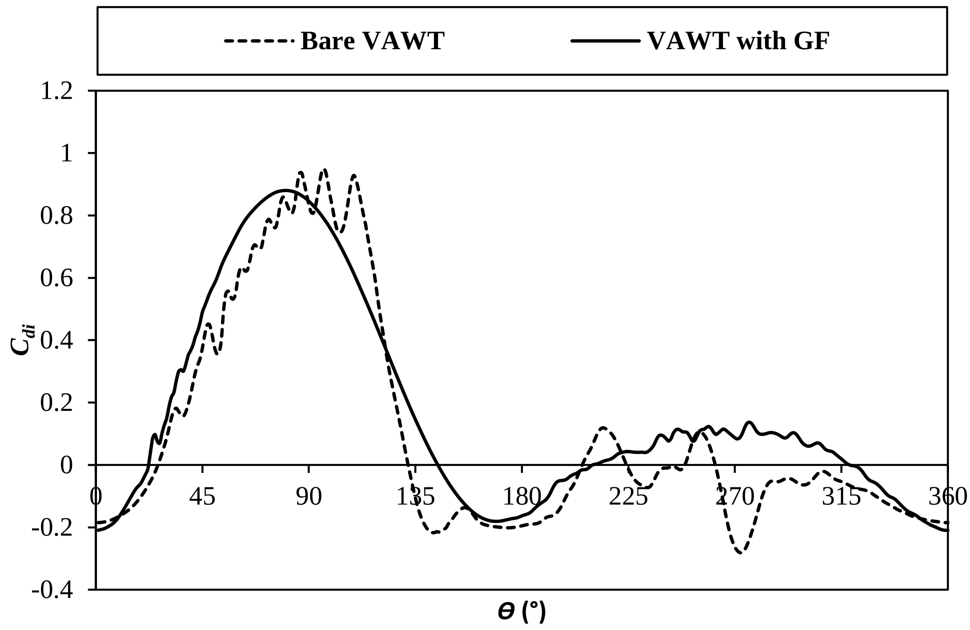

(c)

Figure 5. Comparison of (a) instantaneous moment coefficient, (b) instantaneous lift coefficient and (c) instantaneous drag coefficient respectively, over one rotation cycle of VAWT with GF (optimum geometries) and without GF at *TSR* = 2.64.

Further investigation on the root-mean-square error (RMSE) velocity magnitude contours with super-imposed pathlines (see the right graphs of Figure 6 (a)) reveals that the GF addition can certainly introduce vortices in downstream, which can influence the flow and pressure fields near the trailing edge. Moreover, as shown in Figure 6 (a), contours of the root mean square error of velocity magnitude suggest that the GF can enhance the velocity magnitude over the suction surface whilst decreasing it on the pressure surface. As a result, less flow separation can be seen (showed by less vortex shedding in Figure 6 (b)), and the total circulation of the blade will be increased (consistent with enhanced lift coefficient). For example, the calculation of circulation (Γ) by taking surface area (S) integral of vorticity (ξ) (see Equation 5) of the blades shows that the addition of GF (optimum geometries) can improve the total circulation of the blades of VAWT by about 108% compared to bare VAWT at *TSR* = 2.64 (θ = 90°). Therefore, the lift enhancement will lead to more power generation achieved by using the GF mounted on the blades.

$$\Gamma = \oint \xi . dS, \tag{5}$$

where $\xi = \nabla \times \vec{U} = \frac{\partial U_y}{\partial x} - \frac{\partial U_x}{\partial y}$ with U_y is *y*-velocity component and U_x is *x*-velocity component, respectively.

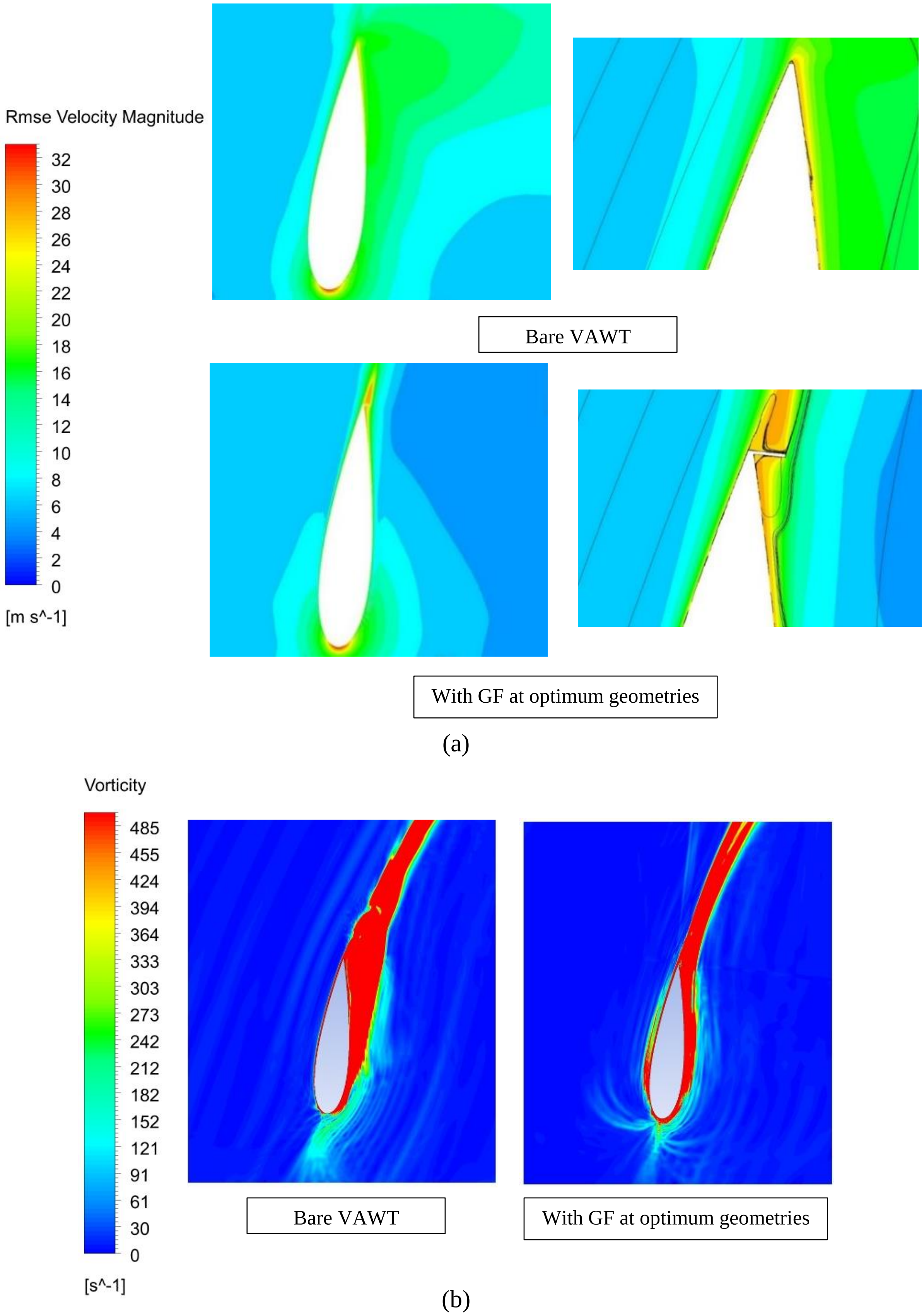

Figure 6. Comparison of (a) root-mean-square error (RMSE) velocity magnitude contours with super-imposed pathlines in the right graphs and (b) contours of *z*-vorticity between bare VAWT and VAWT with GF (optimum geometry) at $TSR = 2.64$, $\theta = 90°$.

Although GF can improve the $C_{p\text{-}ave}$ of bare VAWT at all ranges of *TSR*s, the degree of improvement can be varied at each range of *TSRs*. For example, GF with a height equals to 3% *c*, 90° mounting angle and mounted at the trailing edge of the blade is likely to have a significant influence on the increment of $C_{p\text{-}ave}$ at low ranges of *TSR*s (around 130.94% performance increment compared to a bare VAWT at the lowest value of *TSR*). At medium *TSR*s range, the improvement of $C_{p\text{-}ave}$ of VAWT in the presence of GF is lower compared to low range of *TSR*s (about 69.94% of the optimum *TSR* value of a bare VAWT), whilst at high *TSR*s range, GF can still enhance the $C_{p\text{-}ave}$ (approximately 41.36% at the highest value of *TSR*), but not as significant as those at low and medium ranges of *TSR*s. This phenomenon is most likely caused by the different range of angle of attacks operation and beyond static stall *AoA*s of an aerofoil at those ranges of *TSR*s. As mentioned by Malael et al. [13], the range of *AoA*s operation and beyond static stall *AoA*s works on the blade at low range of *TSR*s more widely than the medium and high ranges of *TSR*s. Hence, the benefit of having a GF to increase the maximum lift and reducing the dynamic stall of VAWT can be utilised effectively at this range of *TSR*s, compared to the medium and high ranges of *TSR*s.

It is also noticed that the presence of GF moves an optimum *TSR* to a lower value compared to bare VAWT (e.g. from *TSR* = 2.64 to *TSR* = 2.50). In fact, this is rather desirable as VAWT can produce optimum power output at lower *TSR*, as higher *TSR* expresses the higher tangential speed at the blade trailing edge resulting in significant and undesirable centrifugal force. Consequently, VAWT will produce a higher noise level and need stronger blades in terms of structure to balance the larger centrifugal force. Therefore, GF will also help VAWT to produce optimum power with a lower noise level and strength requirements of the blade structure.

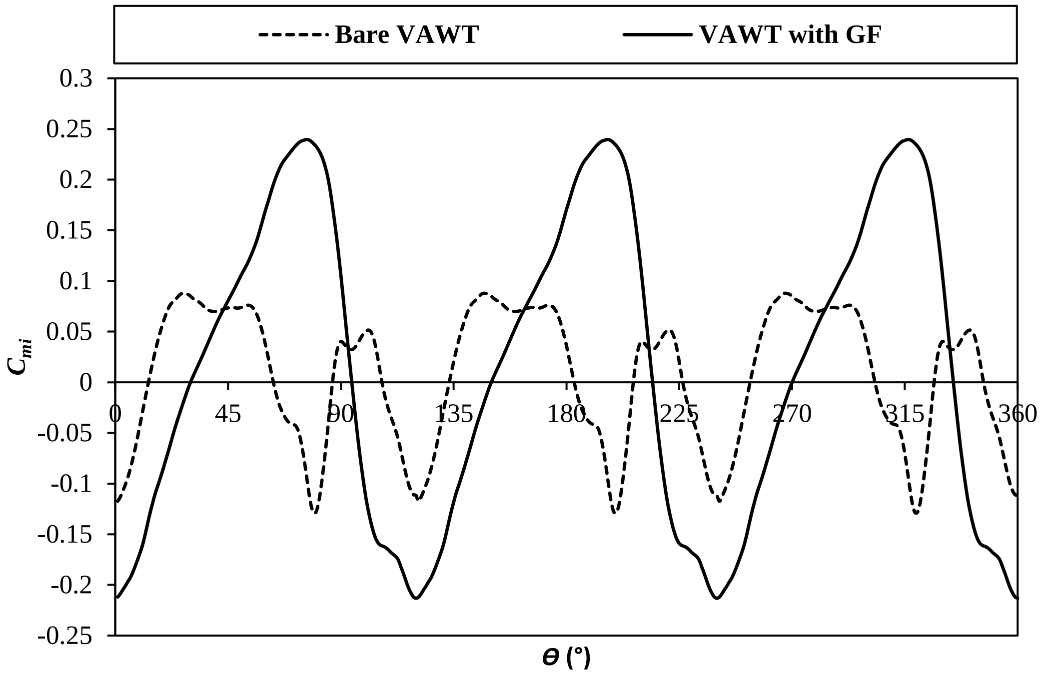

Figure 7. Comparison of C_{mi} distribution of VAWT at *TSR* = 1.44 with GF (H = 3% c, θ_{GF} = 90° and s = 0% c from trailing edge) and without GF.

The use of GF to significantly improve the power generation of VAWT at lower range of *TSR*s is desirable as it can also enhance the self-starting ability of VAWT. It is widely known that at lower range of *TSR*s, VAWT tends to experience dynamic stalls and, therefore, produce a considerable amount of negative moments that prevent the VAWT from rotating by itself. As a result, VAWT operated at a low range of *TSR*s often needs additional external power to rotate the turbines before producing a positive moment for power generation. The addition of GF can reduce the number of positive/negative moment production pairs as indicated with only one negative peak of C_{mi} distribution in every 120° azimuthal position, as seen in Figure 7. This shows that GF can ease dynamic stall at low range of *TSR*s. While adding GF can decrease the number of negative peak C_{mi} compared to bare VAWT, it also enhances the optimum value of C_{mi} significantly. Thus, the presence of GF improves the moment production of VAWT at low range of *TSR*s, and this demonstrates that GF can essentially elevate the self-starting ability of VAWT at this range of *TSR*s.

5.3. Effects of the height of GF

As shown in Figure 4 (a), the $C_{p\text{-}ave}$ of VAWT generally rises with the increase of the GF height, with a maximum $C_{p\text{-}ave}$ achieved for a GF height of 3% c. Further increasing GF height beyond 3% c will lose its capability to further increase the $C_{p\text{-}ave}$. Compared to a single stationary aerofoil with an optimum GF height of 2% *c* [6], this optimum GF height is slightly higher, possibly due to the rotating effect and the wake-blade interactions. Nevertheless, this observation confirms that those findings from a single stationary aerofoil with GF are not applicable to the rotating wind turbine blades scenarios.

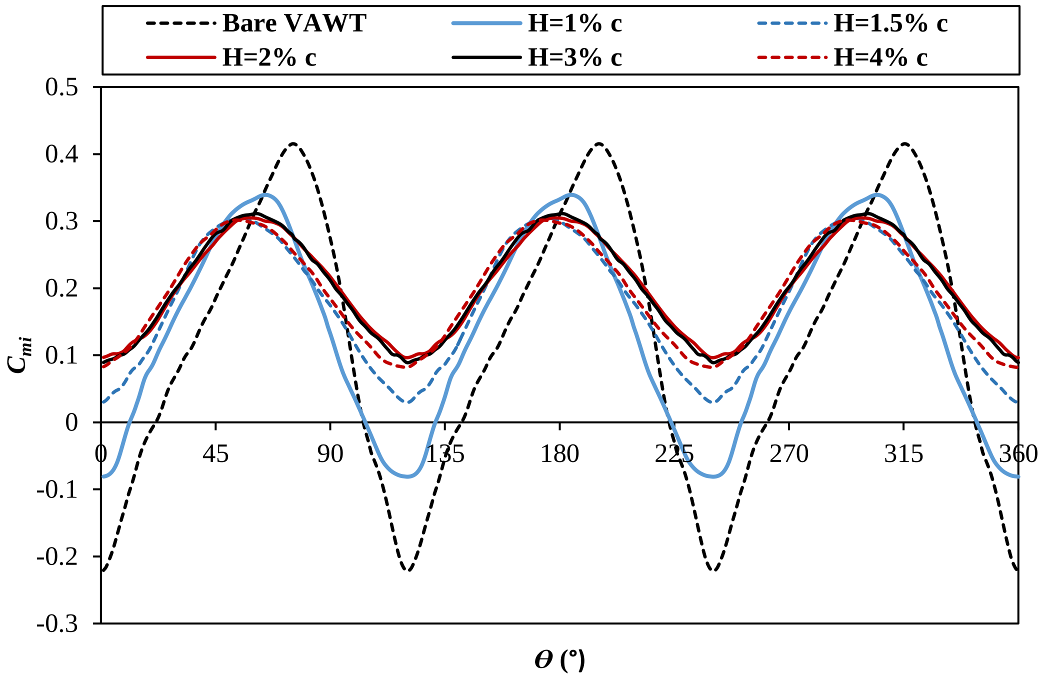

Figure 8. Comparison of C_{mi} distribution of VAWT with and without GF at various GF heights (TSR = 2.64).

Figure 8 illustrates the instantaneous moment coefficients over one turbine revolution from simulations of different GF heights. The C_{mi} distribution demonstrates that a GF with a height equal to or higher than 1.5% *c* can totally remove the negative C_{mi}. As the height of GF increases, the variation values of C_{mi} moves forward to positive values and the average value of C_{mi} increases (For example, averaged C_{mi} increases from 0.1409 for GF with H = 1% *c* to 0.2043 for GF with H = 3% *c*), resulting in an increased power output until an optimum GF height of 3% *c*. After this optimum height, even if there is no negative C_{mi} production, the variation values of C_{mi} shifts down to be negative and thus, the average value of C_{mi} decreases (averaged C_{mi} declines from 0.2043 for GF with H = 3% *c* to 0.1967 for GF with H = 4% *c*). This indicates that when a GF height is greater than 3% *c*, the GF addition starts to reduce the moment production of the turbine. In Figure 8, GF with H = 4% *c* slightly decreases the minimum value of C_{mi} towards the negative value compared to GF with optimum height and, as a result, it decreases the improvement of VAWT performance.

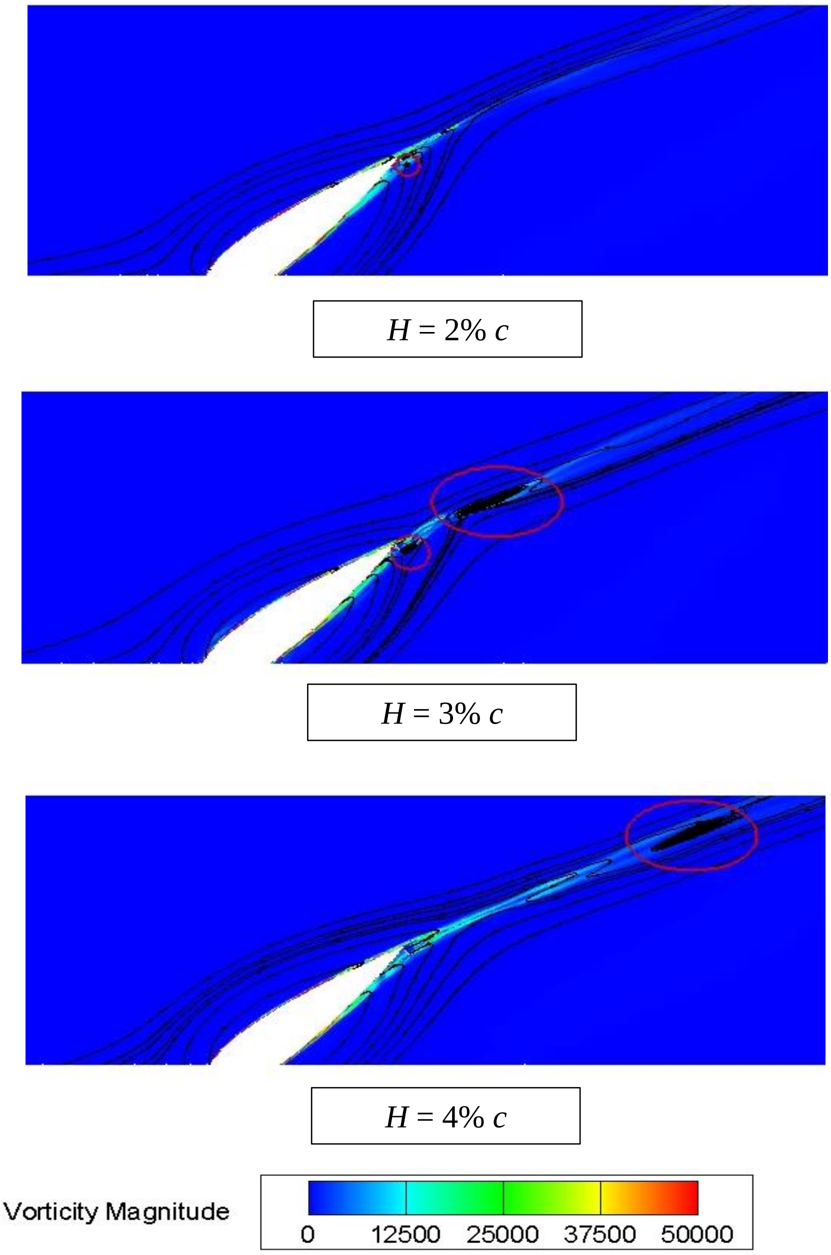

(a)

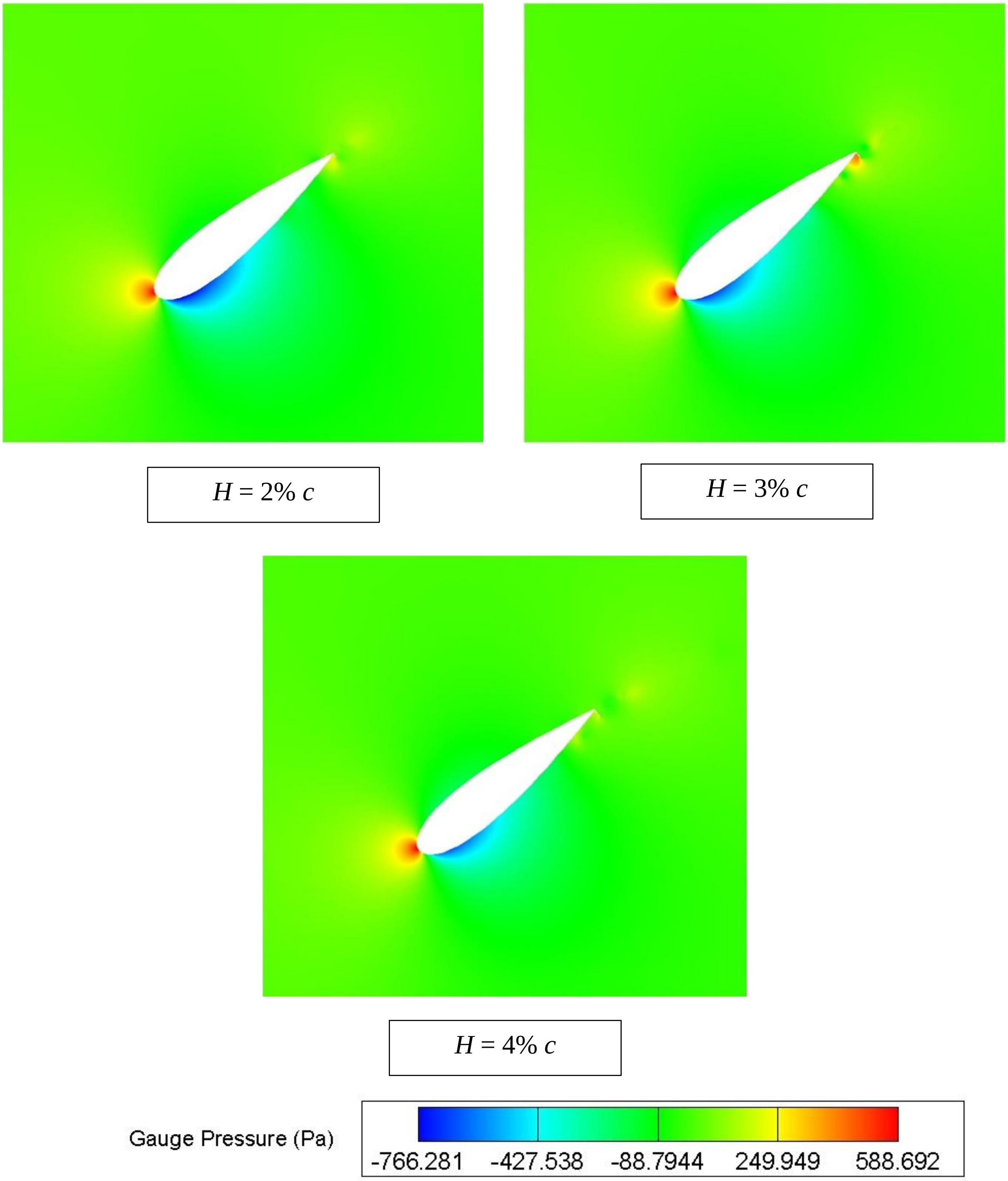
H = 2% c
H = 3% c
H = 4% c
Gauge Pressure (Pa)
-766.281
-427.538
-88.7944
249.949
588.692

(b)

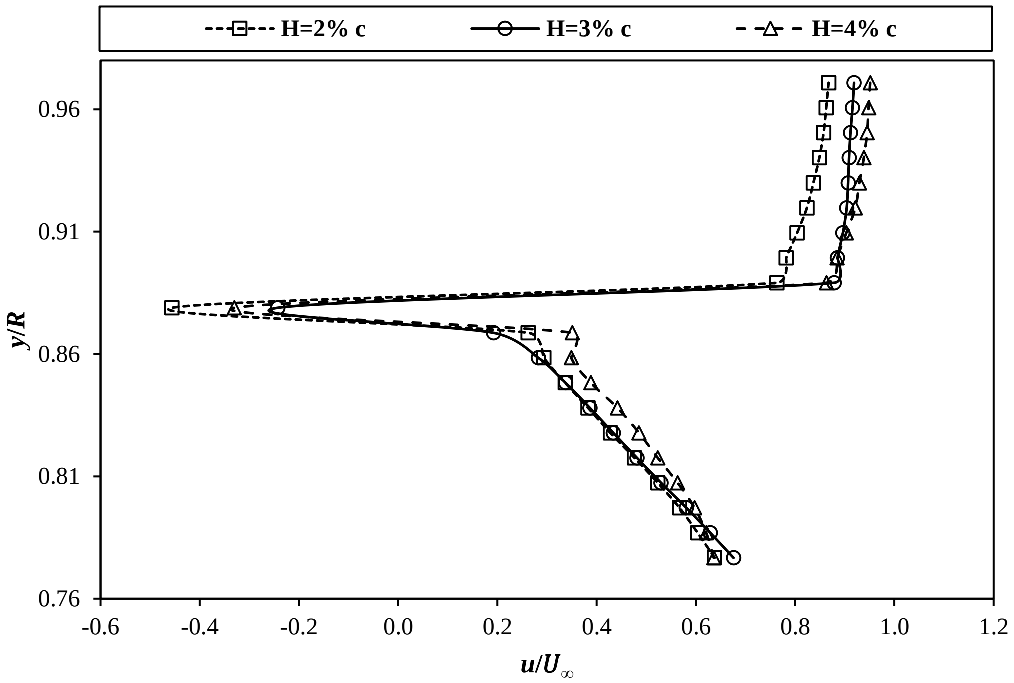

(c)

Figure 9. Comparison of (a) streamlines coloured by *z*-vorticity contours, (b) contours of gauge pressure and (c) *x*-velocity profiles in the wake region of one selected blade (blade 1) at various heights of GF (*TSR* = 2.64, θ = 45°).

Further investigation of streamlines coloured by *z*-vorticity contours (see Figure 9 (a)) at azimuthal position = 45° (i.e., where there is significant difference of C_{mi} between GF with three different heights) indicates that GF with *H* = 3% *c* generates two counter-rotating vortices in the near wake of GF, while GF with *H* = 2% *c* and 4% *c* only generate one vortex in the same wake region (see, e.g. red circles in Figure 9 (a)). These two counter-rotating vortices in downstream of GF lead GF with *H* = 3% *c* to have smaller momentum deficits in the wake region (as shown by narrower *x*-velocity variation in Figure 9 (c)). Hence, the highest increment of lift force generation can be achieved by GF with *H* = 3% *c*. In addition, the gauge pressure contours demonstrate that there is no significant difference in pressure distributions at the leading edge of the blade, showing that GF indeed does not have effect on the flow around leading edge of the blade (see Figure 9 (b)). On the other hand, noticeable difference can be seen around the trailing edge of the blade (in particular at the pressure side of the blade) when the height of GF is altered. Compared to GF with *H* = 2% *c* and 4% *c*, GF with *H* = 3% *c* has shown higher variations in the gauge pressure contours around trailing edge of the blade (see, e.g. colour differences between the suction and pressure sides of the blade). This suggests that GF with *H* = 3% *c* can produce the highest difference in gauge pressure compared to other two heights, resulting in the largest moment production. As a results, GF with H = 3% c can produce the greatest improvement of the power coefficient of VAWT.

Concerning the effect of GF height on the VAWT performance improvement at different ranges of *TSR*s, the effect of GF on the improvement of the power coefficient of VAWT has shown similar trends at all three ranges of low, medium and high *TSR*s, as illustrated in Figure 4 (a). As the GF height increases, the $C_{p\text{-}ave}$ also increases until it reaches an optimum value for a GF with H = 3% c. After that, the $C_{p\text{-}ave}$ decreases, indicating that GF height increment cannot further enhance the $C_{p\text{-}ave}$ of VAWT. For all GF heights that have been tested, it is observed that GF generates the highest $C_{p\text{-}ave}$ increment at low range of *TSR*s, followed by the medium and high range of *TSR*s (see, e.g. Figure 10). This indicates that at those ranges of GF height, the presence of GF has the strongest capability to improve the performance of VAWT at low ranges of *TSR*s. Nevertheless, it has been observed at high range of *TSR*s that whilst a GF with the height of less than or equals to 3% c experiences a similar rate of decrement of the $C_{p\text{-}ave}$ enhancement, a GF with a height greater than 3% c (e.g. 4% c) experiences a significant reduction in $C_{p\text{-}ave}$ improvement. The reason behind this is probably due to the fact that the decrement of lift to drag ratio as the GF height increases could be more prominent at this range of *TSR*s.

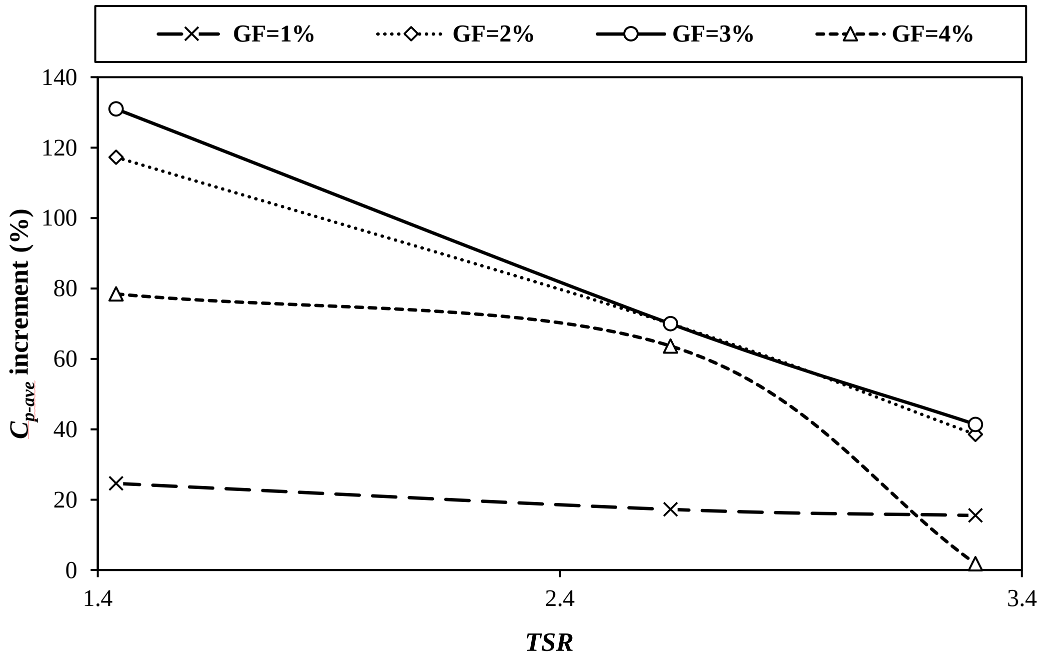

Figure 10. Comparison of $C_{p\text{-}ave}$ improvement of VAWT with GF against GF heights at different ranges of *TSR*s (*TSR* = 1.44 for low ranges of *TSR*s, *TSR* = 2.64 for medium ranges of *TSR*s and *TSR* = 3.3 for high ranges of *TSR*s).

At *TSR* = 2.64 (in medium range of *TSR*s), averaged lift to drag ratio is reduced by about 0.004 whilst GF height increases from 3% c to 4% c. Meanwhile, at *TSR* = 3.3 (in high range of *TSR*s), this value decreases significantly by about 0.0128. As explained above, GF cannot optimally enhance its ability to reducing the dynamic stall of VAWT at high range of *TSR*s, and this is because, at this range of *TSR*s, the increment of $AoAs$ beyond the static stall angle becomes smaller, compared to both the low and medium ranges of *TSR*s. Hence, GF contribution to lift increment decreases (at *TSR* = 3.3, averaged lift decreases from 0.243 to 0.242 whilst GF height increases from 3% c to 4% c) whilst the drag rises (at *TSR* = 3.3, averaged drag increases from 0.1309 to 0.1315 whilst GF height increases from 3% c to 4% c), resulting in a lower lift to drag ratio.

5.4. Effects of the mounting angle of GF

Figure 11 (a) illustrates the effect of variation of GF mounting angle and height at a fixed position (0% *c* from trailing edge) on the $C_{p\text{-}ave}$ of VAWT at *TSR* = 2.64. There are similar tendencies of $C_{p\text{-}ave}$ variations between different GF heights as those GF mounting angle changes. This means that the $C_{p\text{-}ave}$ of VAWT increases with the increase of the GF mounting angle until reaching its optimum value at θ_{GF} = 90°. Beyond this angle, the ability of GF to improve the $C_{p\text{-}ave}$ of VAWT starts to reduce. Nevertheless, VAWT with a GF height lower than 1.5% *c* and a mounting angle larger than 90° (it is 135° in this case) will produce a $C_{p\text{-}ave}$ value lower than that of a bare VAWT. This finding suggests that GF with a shorter height and smaller mounting angle towards the lower surface of the blade will not improve the performance of VAWT.

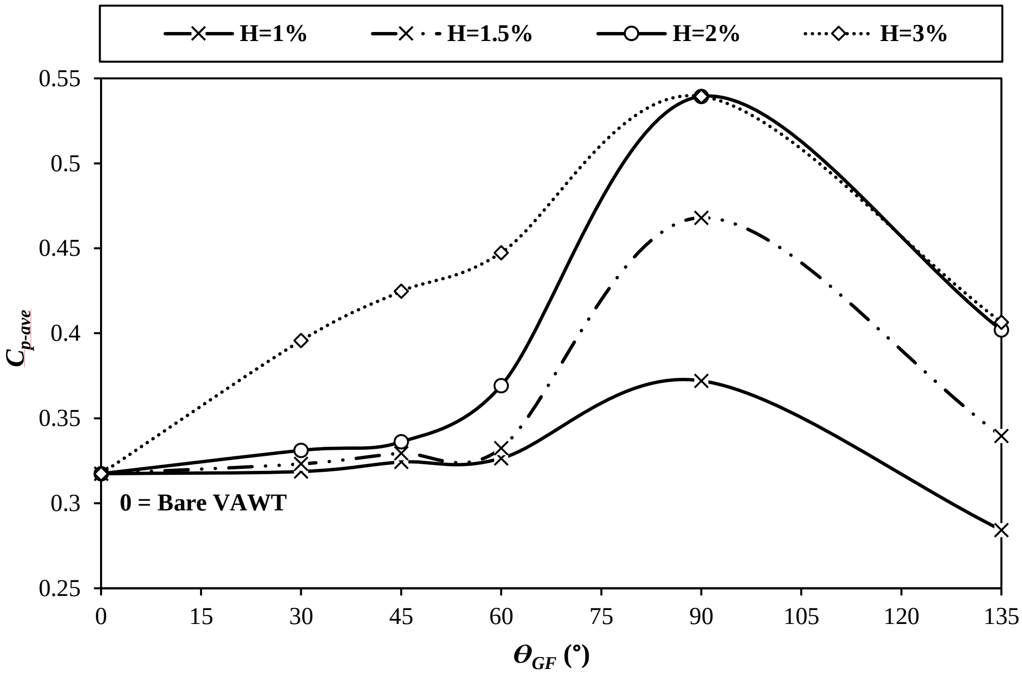

(a)

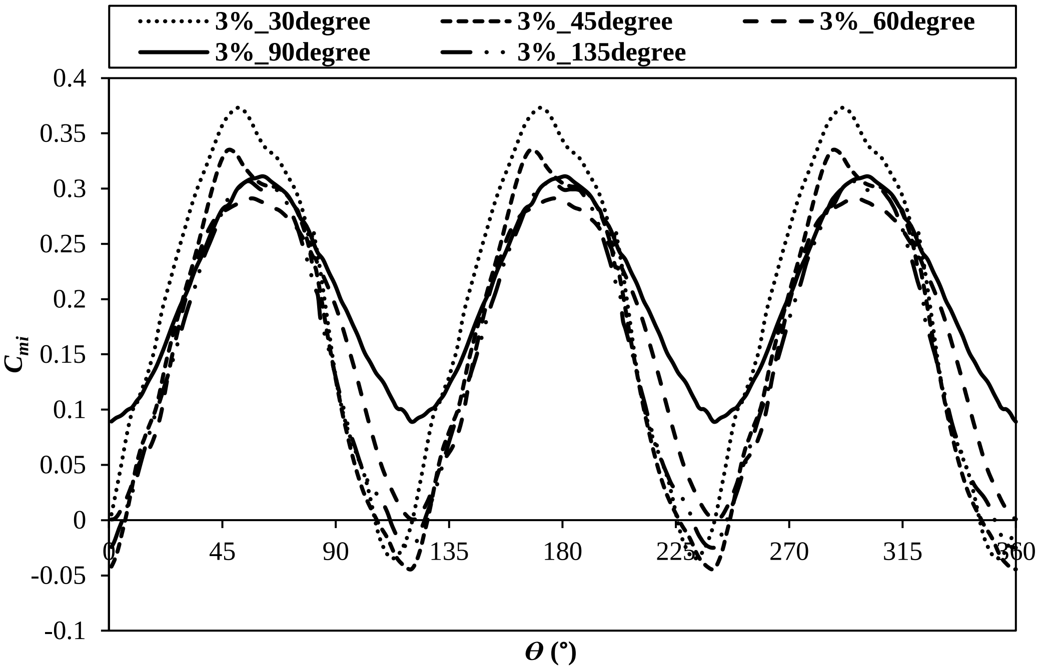

(b)

Figure 11. Comparison of (a) $C_{p\text{-}ave}$ of VAWT with and without GF at various GF heights and mounting angles and (b) C_{mi} distribution of VAWT with GF at various GF mounting angles with a fixed height of 3% c. GF is fixed at 0% c from the trailing edge and TSR = 2.64.

Further investigation of C_{mi} distribution shows that GF with a height equals to 3% c, a distance from trailing edge at 0% c and mounting angles between 60° and 90° or an angle of θ_{GF} = 90° can remove the negative moment production of VAWT, resulting in the highest positive moment production, for TSR = 2.64 (see Figure 11 (b)). The gauge pressure contours (see Figure 12 (b)) at θ = 120° (i.e. where there are significant C_{mi} differences between GF with θ_{GF} = 60°, 90° and 135°) demonstrate that compared to GF with other two mounting angles, GF with θ_{GF} = 90° produces significant higher gauge pressure at the trailing edge of the blade (as indicated by yellow colour shade domination in the trailing edge of the pressure side of the blade). This leads to a better $C_{m\text{-}ave}$ increment for GF with θ_{GF} = 90° than other two mounting angles, resulting in higher $C_{p\text{-}ave}$ value.

Moreover, C_{mi} distribution at θ_{GF} = 90° implies the slowest rate of decrement of C_{mi} and the longest delay of the fall of C_{mi}, indicating that GF mounting angle at θ_{GF} = 90° has the best ability to reduce the dynamic stall experienced by VAWT, and in the meantime increase its lift production. It is further confirmed by the streamlines coloured by z-vorticity contours at θ = 120°. At this azimuthal position, GF with θ_{GF} = 90° generates a small region of reverse flow at the leading edge of the pressure side of the blade compared to GF with other two mounting angles, resulting in relative weaker or even almost invisible vortex shedding behind the trailing edge of the blade (see Figure 12 (a)). On the other hand, GF with θ_{GF} = 60°and 135° induce larger region of reverse flows at the leading edge of the pressure side of the blade. This region is quite large, ranging from the leading edge up to the trailing edge. It causes stronger vortex shedding behind the trailing edge of the blade with increased drag, compared to GF with θ_{GF} = 90° (see Figure 12 (a)). Hence, GF with 90° mounting angle can generate the highest $C_{m\text{-}ave}$ improvement of VAWT, leading to highest $C_{p\text{-}ave}$ value compared to GF with other two mounting angles. This is in an agreement with previous study that mentioned that stronger vortex shedding could increase the drag generation and as a result, reduce the lift to drag ratio and lead to the performance decrement [33].

In relation to the effect of GF mounting angle at different ranges of TSRs, Figure 4 (b) has already shown that the change of range of TSRs does not affect the trend of $C_{p\text{-}ave}$ variation caused by the change of GF mounting angle. At all ranges of TSRs, VAWT produces the highest $C_{p\text{-}ave}$ at θ_{GF} = 90°, indicating that this optimum mounting angle can be applied for all ranges of TSRs.

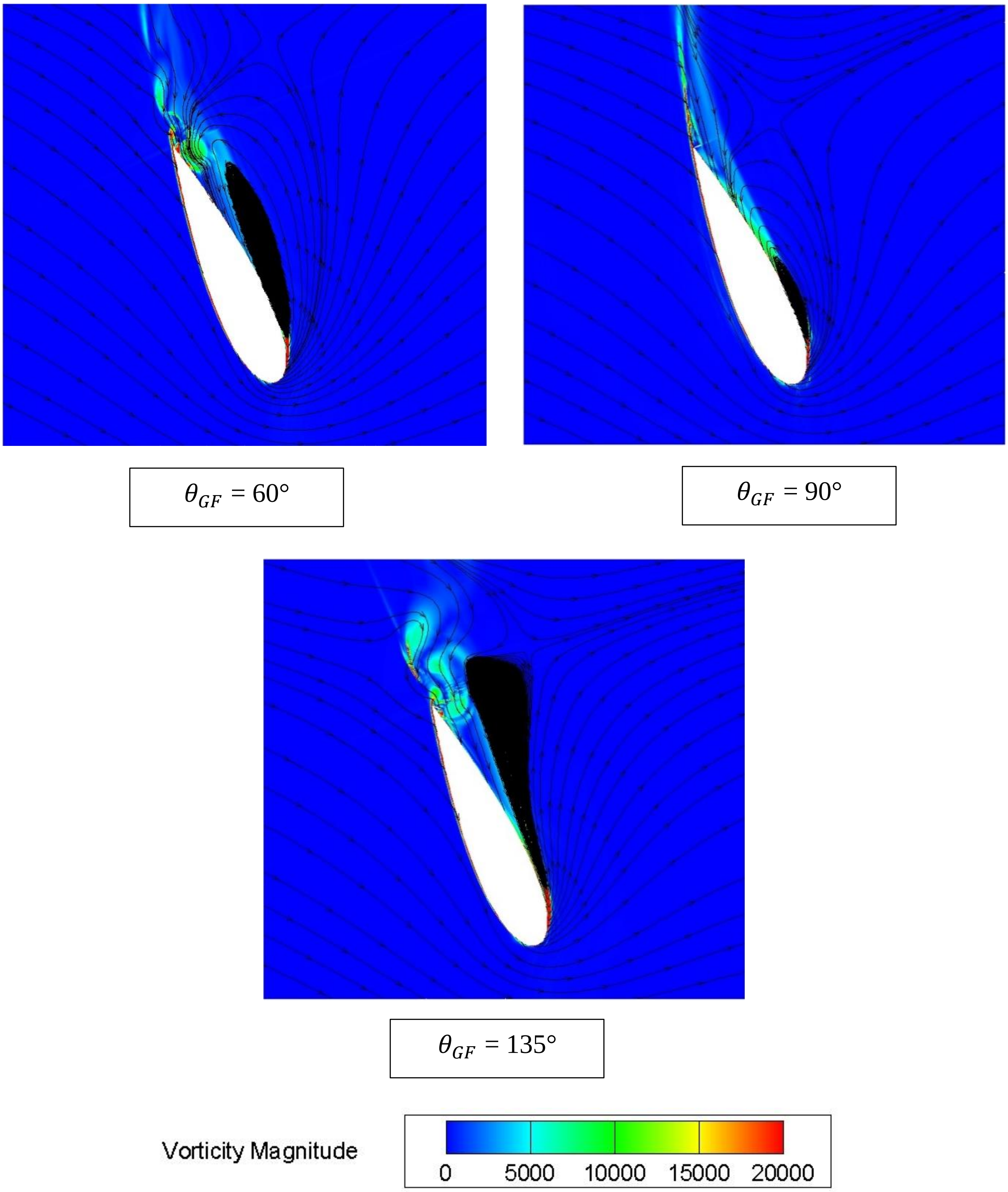
θ_{GF} = 60°
θ_{GF} = 90°
θ_{GF} = 135°
Vorticity Magnitude
0
5000
10000
15000
20000

(a)

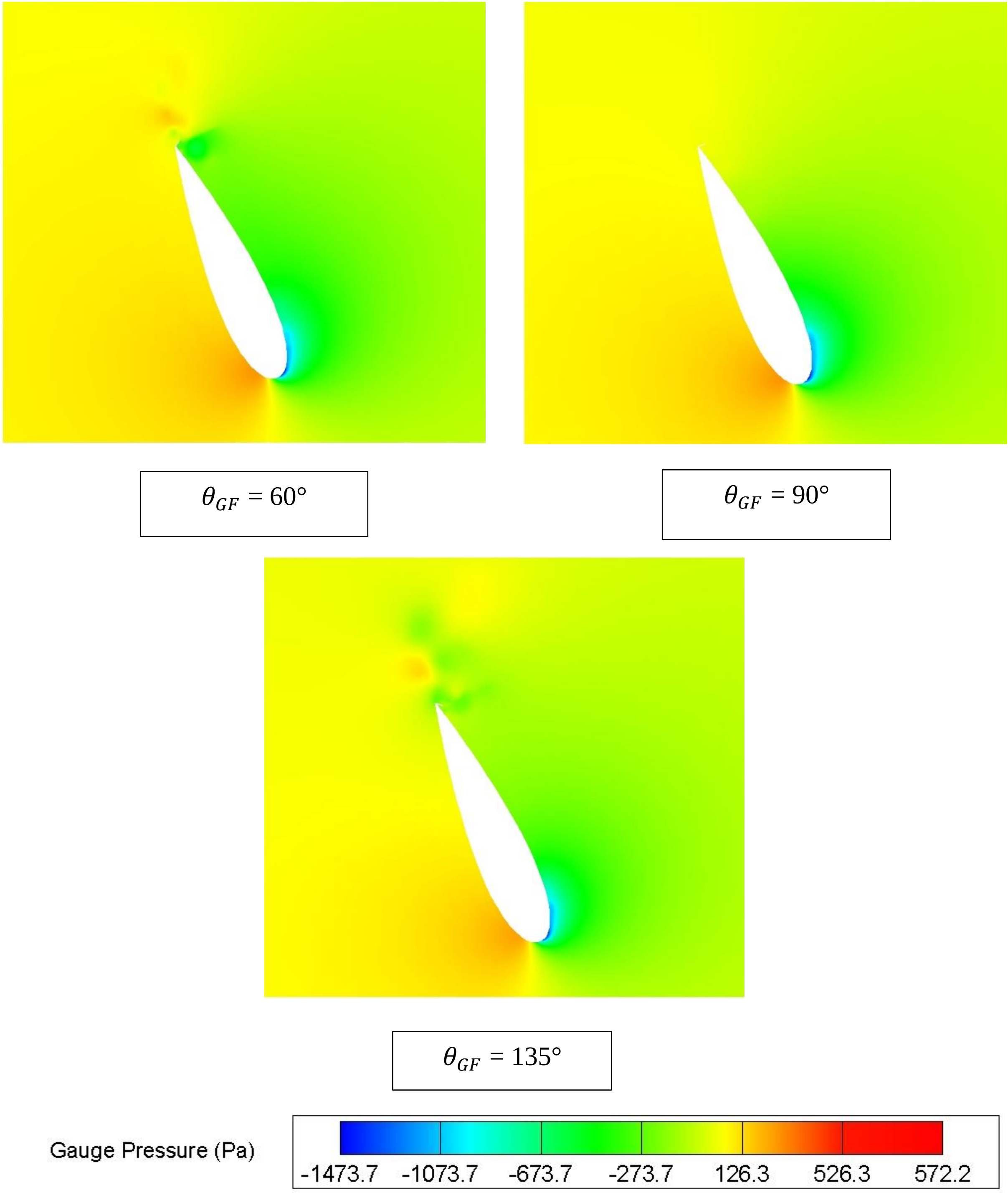

(b)

Figure 12. Comparison of (a) streamlines coloured by *z*-vorticity contours and (b) contours of gauge pressure at various mounting angles of GF (TSR = 2.64, θ = 120°).

5.5. *Effects of the position from the trailing edge of GF*

As illustrated in Figure 4 (c), the GF position will have different effects on the performance of VAWT with GF at different ranges of *TSR*s. At low range of *TSR*s, GF position from the trailing edge less than 4% *c* can improve the $C_{p\text{-}ave}$ production, compared to GF at trailing edge (see Figure 4 (c)). If the GF is moved further than 4% *c* from the trailing edge, the $C_{p\text{-}ave}$ generation starts to decrease, although it is still higher than the bare VAWT. Moving GF position towards the leading edge will likely reduce or even remove the ability of GF to improve the performance of VAWT. Figure 13 (a) shows that by mounting GF further away from the trailing edge (0% c $\leq s \leq$ 4% *c*), GF can further decrease the negative moment production of VAWT, which can improve the power generation VAWT. After $s >$ 4% *c*, this ability starts to be weakened, and optimum moment production has shown lower than those whilst $s \leq$ 4% *c*. Therefore, the $C_{p\text{-}ave}$ generation for GF position > 4% *c* is lower than that GF position of less than 4% c.

Meanwhile, at medium and high ranges of *TSR*s, changing the GF position further away from the trailing edge does not positively influence the increment of $C_{p\text{-}ave}$ (see Figure 4 (c)). The $C_{p\text{-}ave}$ continuously decreases compared to the $C_{p\text{-}ave}$ of VAWT with GF at the trailing edge. The C_{mi} distribution at TSR = 2.64, as shown in Figure 13 (b), suggests a significant drop of optimum C_{mi} when the GF position is shifted from the trailing edge. The C_{mi} distribution also shows mentioned behaviours above for all tested GF positions. Furthermore, GF still maintains its ability to remove negative moments, which can improve the performance of VAWT. Nevertheless, as the GF moves upstream towards the leading edge, the C_{mi} minimum value drops to a lower value. This is probably due the fact that changing the GF position further away from the trailing edge (s = 4% *c*) shifts the two counter-rotating vortices further to the downstream region of the blade. Additionally, GF at s = 4% *c* also generates more vortices at both upstream and downstream of the flap (see Figure 14 (a)). The gauge pressure contours indicate that moving the GF position towards to leading edge of the blade can introduce lower pressure region in the upstream and downstream of the GF (e.g. see green shade colour in front of and behind the GF in Figure 14 (b)), triggering the formation of more vortices. Accordingly, the $C_{m\text{-}ave}$ production of VAWT with GF at s = 4% *c* are lower than VAWT with GF at the trailing edge. Therefore, placing GF further away from the trailing edge only reduces the $C_{p\text{-}ave}$ value of VAWT with GF, although the $C_{p\text{-}ave}$ of a VAWT with GF is still better than the bare VAWT until s = 7% *c*.

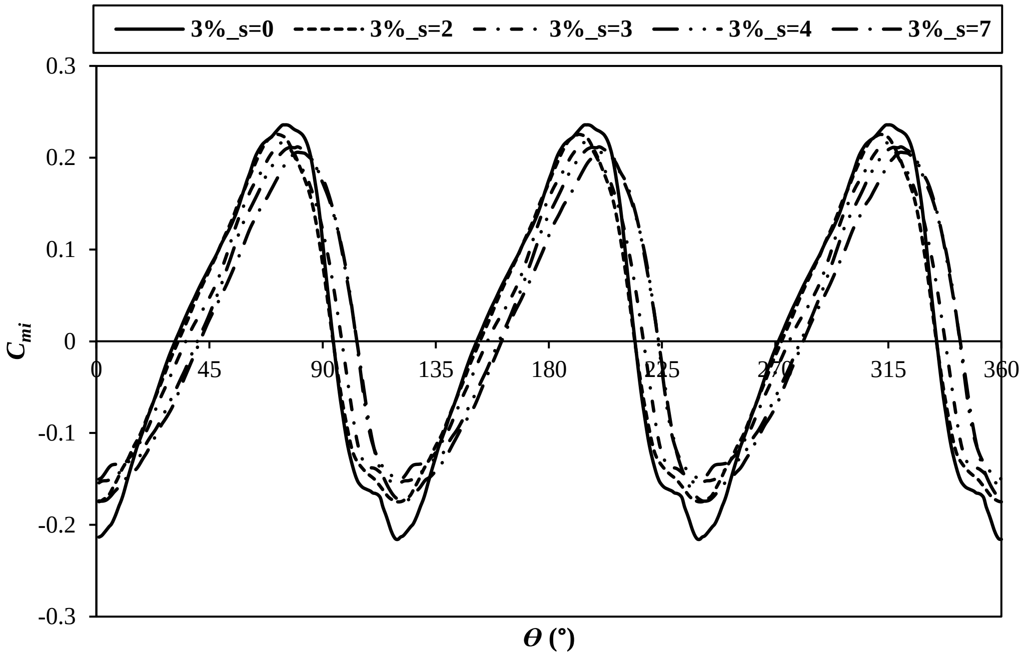

(a)

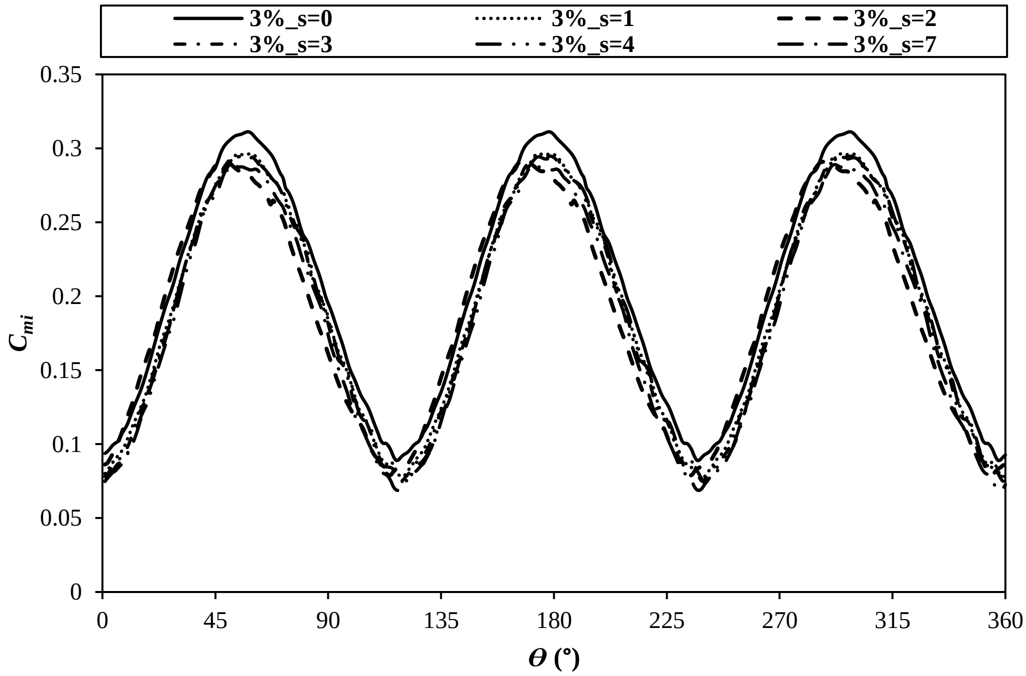

(b)

Figure 13. Comparison of C_{mi} distribution of VAWT with GF at different GF positions, (a) *TSR* = 1.44 and (b) *TSR* = 2.64.

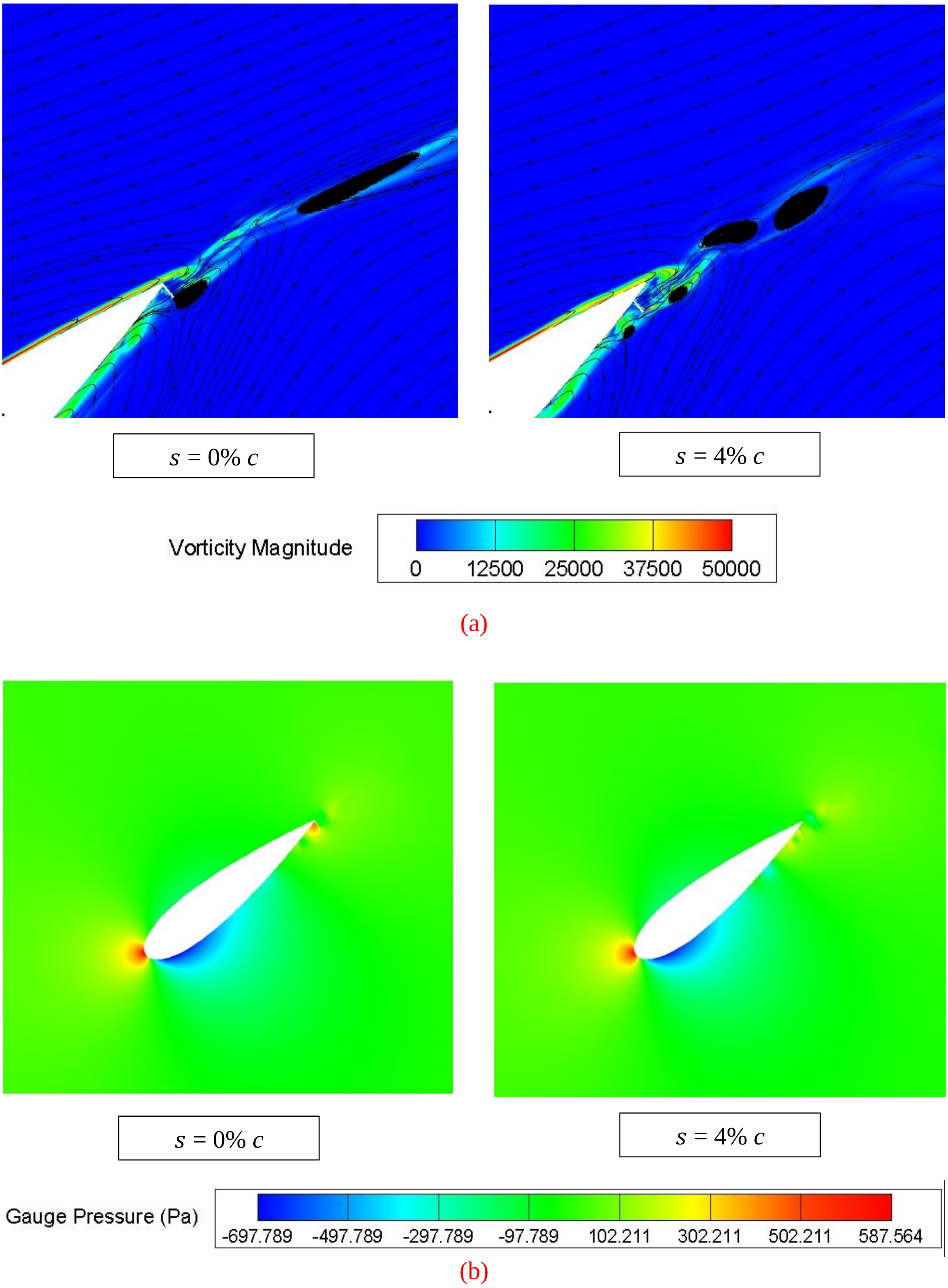

Figure 14. Comparison of (a) streamlines coloured by *z*-vorticity contours and (b) contours of gauge pressure at various GF positions from trailing edge (*TSR* = 2.64, θ = 45°).

The observed difference in the GF position's effect on the $C_{p\text{-}ave}$ improvement between the low range of *TSR*s, and medium and high ranges of *TSR*s can be explained by the streamline distributions at θ = 45° as illustrated in Figure 15 (a). This azimuthal position is chosen as there is significant difference in C_{mi} value between the observed GF's positions at both *TSR*s = 1.44 and 2.64. It demonstrates that for *TSR* = 2.64, the GF position from the trailing edge at *s* = 4% *c* can shift the vortices near downward of the Gurney flap further to the downstream region. In addition, the second vortex, which is located further from the GF, is separated from the newly formed vortex. These newly formed vortices can reduce flow turning over the leeward of the GF, leading to considerable momentum deficits in the wake region (as shown by wider *x*-velocity variation in Figure 15 (b)), and as a result, it reduces the lift force generation. On the other hand, for *TSR* = 1.44, these newly formed vortices do not appear, and there are still two strong counter-rotating vortices at the downstream of GF, which better reduce momentum deficits in the wake region (as shown by narrower *x*-velocity variation in Figure 15 (b)). Hence, the increment of lift force generation still can be achieved.

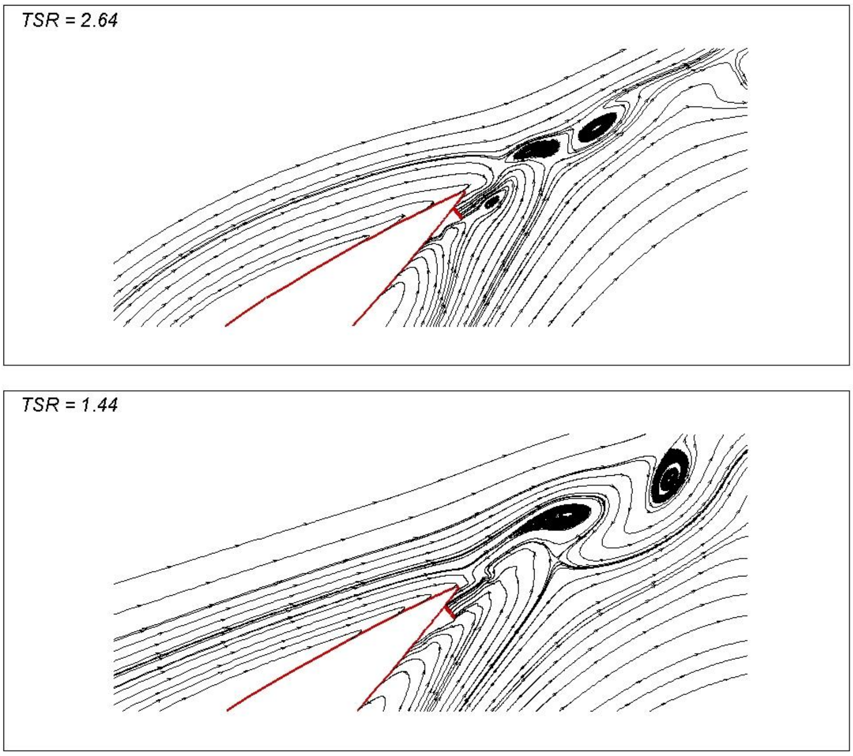

(a)

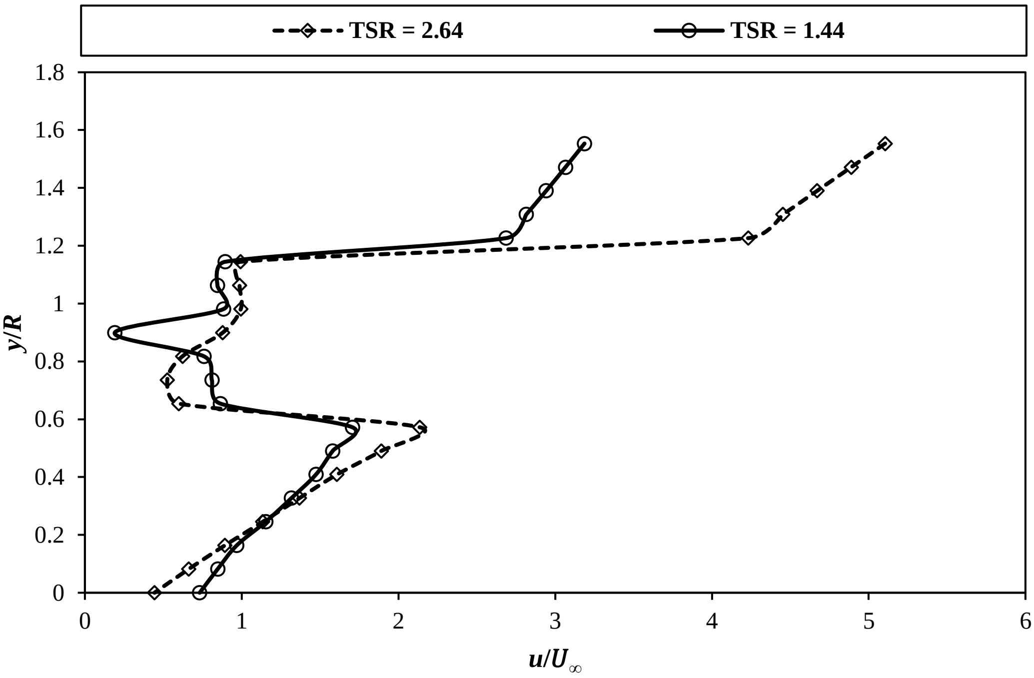

(b)

Figure 15. Comparison of (a) streamlines distribution of VAWT with GF at *s* = 4% of *c* from trailing edge and (b) *x*-velocity profile in the wake region of one selected blade (blade 1) of VAWT with GF mounted at *s* = 4% *c* from trailing edge between *TSR* = 2.64 and *TSR* =1.44 (at θ = 45°).

6. Conclusion

The effect of GF and its geometry optimisation for the VAWT performance enhancement at all ranges of *TSR*s have been studied by hybrid RANS-LES CFD simulations. It is evident that GF geometry optimisation needs to be done for a practical VAWT configuration, particularly rotating multiple blades rather than a single stationary aerofoil. It is found that the VAWT equipped with GF will have an optimum height of *H* = 3% *c*, compared to a single stationary aerofoil with GF, which usually has an optimum height of *H* = 2% *c*. This is probably due to the rotating effect hindering the vortices generation at the upstream of the flap for VAWT with GF.

Overall, VAWT equipped with GF can improve the performance compared to bare VAWT at all ranges of *TSR*s. This confirms that GF can be applied as a passive device to improve the performance of VAWT for whole *TSR*s ranges. Nevertheless, the degree of the VAWT performance improvement caused by GF addition is varied at each range of *TSR*s. The GF has shown the most significant effect at low ranges of *TSR*s (e.g. the C_{p-ave} increment can be up to 233.19% compared to a bare VAWT). It also can improve the self-starting ability at this range of *TSR*s as GF can decrease negative moment production of VAWT and reduce the moment fluctuation, meaning that GF can ease the dynamic stall at this range of *TSR*s. Meanwhile, the level of VAWT performance improvement starts to decrease at medium range of *TSR*s (e.g. $C_{p\text{-}ave}$ increment is up to 69.94% at *TSR* = 2.64, compared to a bare VAWT) and at high range of *TSR*s, this rate is further reduced (e.g. $C_{p\text{-}ave}$ increment is up to 41.36% at *TSR* = 3.3, compared to bare VAWT). This is possibly because the range of $AoAs$ operation and beyond static stall $AoAs$ ($AoAs$ that higher than stall $AoAs$ of static aerofoil) acting on the blades becomes wider with the decrease of *TSR*s. Hence, the benefit of VAWT with GF in increasing the maximum lift and reducing the dynamic stall of VAWT can be utilised more effectively at low range of *TSR*s.

Regarding to the geometry optimisation, it is essential to evaluate at all ranges of *TSR*s. It is found that whilst GF has the same optimum height and mounting angle (i.e. H = 3% c and θ_{GF} = 90°) at all ranges of *TSR*s, there is still a difference in optimum position from the trailing edge between low range of *TSR*s and medium and high ranges of *TSR*s. At a low range of *TSR*s, the $C_{p\text{-}ave}$ value reaches its optimum value whilst the GF has optimum height and mounting angle and is located at s = 4% c. Meanwhile, moving the position of GF towards the leading edge of the blade reduces the $C_{p\text{-}ave}$ generation at medium and high ranges of *TSR*s. Hence, the optimum position of GF at the medium and high ranges of *TSR*s is at the trailing edge of the blade (i.e. s = 0% c). The flow visualisation shows that whilst changing the position of GF at low range of *TSR*s can introduce stronger counter-rotating vortices at downstream of the flap, this behaviour does not happen at the other two higher ranges of *TSR*s.

In conclusion, to generate a relatively higher average performance enhancement at all ranges of *TSR*s, the optimal GF geometry will have a height of 3% c, a mounting angle of 90° and be positioned at the trailing edge of the blade. VAWT equipped with this GF geometry can produce optimum $C_{p\text{-}ave}$ enhancement at medium and high ranges of *TSR*s (i.e. 69.94% and 41.36%, respectively) and retain very high $C_{p\text{-}ave}$ improvement at low range of *TSR*s (i.e. 130.94%). A further experimental study would be valuable to provide test data in validating flow behaviour around VAWT with GF predicted by CFD simulations, so that a better understanding of the actual flow phenomenon around VAWT with GF can be achieved. However, it is outside the scope of this work and can be defined as part of future studies.

Acknowledgement

The first author would like to acknowledge the Ministry of Education, Culture, Research and Technology of Indonesia and Indonesian Endowment Fund for Education (LPDP) of the Ministry of Finance of Indonesia for the financial support through BUDI LPDP scholarship (Reference Letter Number: S-1166/LPDP.3/2017).

References

[1] A. Shires, “Design optimisation of an offshore vertical axis wind turbine,” in *Proceedings of the Institution of Civil Engineers - Energy*, 2013.

[2] I. Malael, R. Bogateanu and H. Dumitrescu, “Theoretical performances of double Gurney Flap equipped the VAWTs,” *INCAS BULLETIN*, vol. 4, no. 4, pp. 93-99, 2012.

[3] H. Zhu, W. Hao, C. Li and Q. Ding, “Numerical study of effect of solidity on vertical axis wind turbine with Gurney flap,” *Journal of Wind Engineering and Industrial Aerodynamics*, vol. 186, pp. 17-31, 2019.

[4] A. Bianchini, F. Balduzzi, D. D. Rosa and G. Ferrara, “On the use of Gurney Flaps for the aerodynamic performance augmentation of Darrieus wind turbines,” *Energy Conversion and Management*, vol. 184, pp. 402-415, 2019.

[5] Y. Yan, E. Avital and J. Williams, “CFD Analysis for the Performance of Gurney Flap on Aerofoil and Vertical Axis Turbine,” *International Journal of Mechanical Engineering and Robotics Research*, vol. 8, no. 3, pp. 385-392, 2019.

[6] Y. Yan, E. Avital, J. Williams and J. Cui, “Performance improvements for a vertical axis wind turbine by means of Gurney Flap,” *Journal of Fluids Engineering*, vol. 142, no. 2, Paper ID 021205, 15 pages, 2020.

[7] E. Sobhani, M. Ghaffari and M. J. Maghrebi, “Numerical investigation of dimple effects on darrieus vertical axis wind turbine,” *Energy*, vol. 133, pp. 231-241, 2017.

[8] A. Choudhry, M. Arjomandi and R. Kelso, “Methods to control dynamic stall for wind turbine applications,” *Renewable Energy*, vol. 86, pp. 26-37, 2016.

[9] Y. Yan, E. Avital, J. Williams and J. Cui, “CFD analysis for the performance of micro-vortex generator on aerofoil and vertical axis turbine,” *Journal of Renewable and Sustainable Energy*, vol. 11, no. 4, Paper ID 043302, 2019.

[10] Z. Wang and M. Zhuang, “Leading-edge serrations for performance improvement on a vertical-axis wind turbine at low tip-speed-ratios,” *Applied Energy*, vol. 208, pp. 1184-1197, 2017.

[11] T.-t. Zhang, M. Elsakka, W. Huang, Z.-g. Wang and D. B. Ingham, “Winglet design for vertical axis wind turbines based on a design of experiment and CFD approach,” *Energy Conversion and Management*, vol. 135, pp. 712-726, 2019.

[12] M. R. Castelli, A. Englaro and E. Benini, “The Darrieus wind turbine: Proposal for a new performance prediction model based on CFD,” *Energy*, vol. 36, pp. 4919 - 4934, 2011.

[13] I. Malael, H. Dumitrescu and V. Cardos, “Numerical simulation of vertical axis wind turbine at low speed ratios,” *Global Journal of Researches in Engineering: I Numerical Methods*, vol. 14, no. 1, pp. 9-20, 2014.

[14] K. Dixon, “The Near Wake Structure of a Vertical Axis Wind Turbine”, Master Thesis ed., Delft: Delft University of Technology, 2008.

[15] M. Bakırcı and S. Yılmaz, “Theoretical and computational investigations of the optimal tip-speed ratio of horizontal-axis wind turbines,” *Engineering Science and Technology, an International Journal*, vol. 21, no. 6, pp. 1128-1142, 2018.

[16] M. Ragheb and A. M. Ragheb, “Wind Turbine Theory - The Betz Equation and Optimum Rotor Tip Speed Ratio,” in *Fundamental and Advanced Topics in Wind Power*: Rijeka, Croatia, InTech, 2011, pp. 19-38.

[17] S. Jain, N. Sitaram and S. Krishnaswamy, “Computational investigations on the effects of Gurney Flap on airfoil aerodynamics,” *International Scholarly Research Notice*, Paper ID 402358, 11 pages, 2015.

[18] M. Cavazzuti, “Optimisation methods: from theory to design scientific and technological aspects in mechanics”, Springer Science & Business Media, 2012.

[19] K. Qasemi and L. N. Azadani, "Optimisation of the power output of a vertical axis wind turbine augmented with a flat plate deflector,” *Energy*, vol. 202, Paper ID 117745, 2020.

[20] Z. Wang, Y. Wang and M. Zhuang, “Improvement of the aerodynamic performance of vertical axis wind turbines with leading-edge serrations and helical blades using CFD and Taguchi method,” *Energy Conversion and Management*, vol. 177, pp. 107-121, 2018.

[21] T. Zou, H. Li, H. Wu, L. Hu and M. Cai, "Design of experiment in analysing uncertainty of simulation results in accident reconstruction," *Proceedings of the Institution of Mechanical Engineers, Part D: Journal of Automobile Engineering*, vol. 233, no. 4, pp. 836-850, 2019.

[22] A. Rezaeiha, H. Montazeria and B. Blockena, “Towards accurate CFD simulations of vertical axis wind turbines at different tip speed ratios and solidities: Guidelines for azimuthal increment, domain size and convergence,” *Energy Conversion and Management*, vol. 156, pp. 301-316, 2018.

[23] “Ansys Fluent User's Guide,” ANSYS Inc, [Online]. Available: https://ansyshelp.ansys.com/account/secured?returnurl=/Views/Secured/corp/v194/flu_ug/flu_ug.html. [Accessed 02 11 2020].

[24] M. Mohammadi, A. Doosttalab and M. Doosttalab, “The effect of various Gurney Flap shapes on the performance of wind turbine airfoils,” in A*SME Early Career Technical Conference (ASME ECTC)*, Georgia, USA, 2012.

[25] H. Zhu, W. Hao, C. Li and Q. Ding, “Simulation on flow control strategy of synthetic jet in a vertical axis wind turbine,” Aerospace Science and Technology, vol. 77, pp. 439-448, 2018.

[26] T. P. Syawitri, Y. F. Yao, J. Yao and B. Chandra, “Assessment of stress-blended eddy simulation model for accurate performance prediction of vertical axis wind turbine,” *International Journal of Numerical Methods for Heat & Fluid Flow*, vol. 31, no. 2, pp. 655-673, 2020.

[27] F. Menter, “Stress-blended eddy simulation (SBES) - A new paradigm in hybrid RANS-LES modeling,” *Notes on Numerical Fluid Mechanics and Multidisciplinary Design*, vol. 137, pp. 27-37, 2018.

[28] T. Frank and F. Menter, “Validation of URANS SST and SBES in ANSYS CFD for the turbulent mixing of two parallel planar water jets impinging on a stationary pool,” in *ASME 2017 Verification and Validation Symposium*, Las Vegas, Nevada, USA, 2017.

[29] T. P. Syawitri, Y. F. Yao, B. Chandra and J. Yao, “Comparison study of URANS and hybrid RANS-LES models on predicting vertical axis wind turbine performance at low, medium and high tip speed ratio ranges,” *Renewable Energy*, vol. 168, pp. 247-269, 2021.

[30] F. Balduzzi, A. Bianchini, R. Maleci, G. Ferrara and L. Ferrari, “Critical issues in the CFD simulation of Darrieus wind turbines,” *Renewable Energy*, vol. 85, pp. 419-435, 2016.

[31] A. Rezaeiha, H. Montazeri and B. Blocken, “On the accuracy of turbulence models for CFD simulations of vertical axis wind turbines,” *Energy*, vol. 180, pp. 838-857, 2019.

[32] T. P. Syawitri, Y. Yao, J. Yao and B. Chandra, “The effect of gurney flap on flow characteristics of vertical axis wind turbine,” *International Journal of Modern Physics B*, vol. 34, no. 14n16, Paper ID 2040107, 2020.

[33] J. Nedić and J.C. Vassilicos, “Vortex shedding and aerodynamic performance of an airfoil with multi-scale trailing edge modifications,” *AIAA Journal*, vol. 53, no. 11 pp. 3240-3250, 2015.